UNIVERSITY OF OKLAHOMA
GRADUATE COLLEGE

EFFECT OF SUB-SATURATION OXYGEN LEVEL IN CANCER CELL GROWTH AND METASTATIC MARKER EXPRESSION

A THESIS
SUBMITTED TO THE GRADUATE FACULTY
in partial fulfillment of the requirements for the
Degree of
MASTER OF SCIENCE

By
JULIANNA HARTWICK
Norman, Oklahoma
2025

Downloaded from SHAREOK. Persistent Handle URL: https://hdl.handle.net/11244/341566

EFFECT OF SUB-SATURATION OXYGEN LEVEL IN CANCER CELL GROWTH AND METASTATIC MARKER EXPRESSION

A THESIS APPROVED FOR THE
STEPHENSON SCHOOL OF BIOMEDICAL ENGINEERING

BY THE COMMITTEE CONSISTING OF

Dr. Vassilios Sikavitsas, Chair

Dr. Roger H. Harrison, Member

Dr. Matthias U. Nollert, Member

© Copyright by JULIANNA HARTWICK 2025
All Rights Reserved.

Acknowledgements

First, I would like to thank my family and the friends who became family over the years. Thank you to my mom, Diane Hartwick, who supported me through this journey, taking every call no matter the hour and moving mountains to be there for me no matter the request. I would like to thank my dad, Pete Hartwick, for all the encouragement and exposure to engineering. To my Grandma Ann Hartwick, for the opportunity to continue my education. Additionally, I would like to thank Bruce and Joan Vance and John and Jill Buchert for always believing in my goals, the continuous check-ins, and guidance in life. All of whom have been my rock and guidepost.

I want to thank the staff and faculty of the Stephenson School of Biomedical Engineering and the School of Sustainable Chemical, Biological, and Material Engineering. I owe many thanks to my advisor Dr. Vassilios Sikavitsas, who not only guided my research, education, and opportunities to develop my technical skills, but also in life. A special thanks to Dr. Roger Harrison, Dr. Matthias U. Nollert, and Dr. Vivek Bajpai for the guidance through my academic experience.

Additionally, I would like to thank the other graduate students who helped answer and support my questions, while inspiring me to investigate the ever-growing field of biomedical engineering. These students include Paige Frey, Kylie Foster, Sampurna Chakraborty, Dr. Federico Flores Arce, Arjun Chakraborty, and Dr. Pradumn Rajvanshi. Additionally, I would like to extend a very special thank you to Parker Bryant, who provided guidance and support to my seemingly endless stream of questions. Lastly, I would like to thank Natalie Norton for all support during the late nights, new endeavors, and for keeping me sane.

Table of Contents

Acknowledgements ..... **iv**

Table of Tables ..... **vii**

Table of Figures ..... **vii**

Abstract ..... **viii**

1. Background and Significance **1**

1.1 Impact of Cancer and Cancer Research 1

1.2 2D Cell Culture Platforms 3

1.2.1 Clinical Drug Efficacy and 2D Cultures *3*

1.2.2 2D Culture versus 3D Culture and In Vivo Models *4*

1.2.3 Complex In Vitro Cultures in Tissue Engineering and Cancer Research *6*

1.3 Significance of Bioreactor Platforms 9

1.3.1 Current Bioreactor Platforms *9*

1.3.2 Flow-Perfusion Bioreactors *12*

1.4 Research Objectives 14

1.4.1 Objective 1 ..... *14*

1.4.2 Objective 2 ..... *14*

2. Cancer Growth and Metastatic Marker Expression in Sub-Saturation Flow-Perfusion Bioreactor System **15**

Summary 15

2.1 Introduction 16

2.1.1 Pathophysiology and Solid Tumor Microenvironment *17*

2.1.2 Hypoxia in Cancer *21*

2.2 Methods 25

2.2.1 Cell Culture *25*

2.2.2 3D-Printed Poly-L-Lactic Acid Cassette Holder Production *25*

2.2.3 Oxygen Sensor Assembly *26*

2.2.4 Bioreactor Assembly *27*

2.2.5 Hydrogel Formation *32*

2.2.6 Oxygen Data Collection *33*

2.2.7 Oxygen Sensor Calibration *35*

2.2.8 Oxygen Uptake Calculations *36*

2.2.9 Hydrogel Dimension Measurement *37*

2.2.10 Estimation of Anoxic Core Region *37*

2.2.11 Cellular Quantification *40*
2.2.12 Gene Expression *41*
2.2.13 Statistical Analysis *42*
2.3 Results 43
2.3.1 Measured Oxygen Saturation and Oxygen Uptake *43*
2.3.2 Cell Growth and Viability *48*
2.3.3 Hydrogel Dimensions and Anoxic Core Estimation *51*
2.3.4 Gene Expression *57*
2.4 Discussion 59
2.5 Conclusion 65
2.6 References 67

Table of Tables

Table 2.1: Gene Primer Sequences 42

Table 2.2: Hydrogel Dimensions and Volume 51

Table of Figures

Figure 2.1: Solid Tumor Microenvironment 19

Figure 2.2:PLLA Hydrogel Scaffold Holder 26

Figure 2.3:OxyMod Sensor Assembly 27

Figure 2.4: General Bioreactor Schematic 28

Figure 2.5: Cross Sectional View of One Bioreactor Chamber 28

Figure 2.6: Series Bioreactor Configuration 30

Figure 2.7: Parallel Bioreactor Configuration 31

Figure 2.8: Anoxic Core Estimation Diagram 40

Figure 2.9: Oxygen Saturation of Series and Parallel Configuration 45

Figure 2.10: Oxygen Consumption per Scaffold 46

Figure 2.11: Oxygen Uptake Rate per Cell 47

Figure 2.12: Percent Growth of Cell Scaffolds 49

Figure 2.13: Percent Viability of Scaffolds 50

Figure 2.14: Percent Volume Change of Hydrogel Scaffolds 53

Figure 2.15: Estimated Depth to Anoxic Core Region of Hydrogel Scaffold 55

Figure 2.16: Model Predicted Percentage of Anoxic Volume 56

Figure 2.17: Genetic Expression of Hypoxia and Disease Progression Genes 58

Abstract

Cancer remains a leading cause of death worldwide, with incident rates projected to increase. Although mortality rates have improved, a cancer diagnosis remains a significant burden for patients and their families. This burden extends beyond psychological and physical hardships, but also economic strain. For example, the economic cost of cancer treatment is estimated to reach approximately 25.2 trillion international dollars. Contributing to these rising costs is the limited clinical success of modern therapeutics, which restricts their introduction and drives the cost of successful therapeutics.

One of the responses includes the field of tissue engineering has expanded into cancer research. The current *in vitro* cancer culture models generally rely on traditional 2D monolayer cell culture. This method lacks the native cell conformation, function, and physiological accuracy. Additionally, many therapeutic screenings appear promising in the pre-clinical research stage but ultimately fail to translate into clinical trials due to these oversimplifications. Furthermore, the nude mouse models lack critical immune response components. As the newer therapeutics are shifting from cytotoxic drugs to immunotherapeutics, nude mouse models are losing effectiveness. Thus, there is a demand for novel, more accurate *in vitro* cancer research models. Tissue engineering allowed the development of 3D cellular structures that satisfy many of the criteria required in *in vitro* cancer research models but necessitate special culturing conditions. Bioreactors are becoming increasingly popular in the field of tissue engineering and are great candidates to fill this void. Flow-perfusion bioreactors in particular are uniquely suited to create 3D macro-scale cell culture environments with the additional benefit of mechanical stimulation when needed. Culture conditions can be monitored through modular sensors in the liquid phase and gas phase, which provides a method for real time monitoring.

The cellular physiological limitations of traditional 2D culture models led to the guiding questions of this thesis: 1) “In which ways do sub-saturation of oxygen levels affect the proliferation, oxygen uptake, and phenotypic modification of cancer cells in 3D *in vitro* culture with flow-perfusion bioreactor models?” and 2) “How does sub-saturation oxygen levels drive metastatic markers in 3D cancer models?”. These questions will be addressed by utilizing a previously modified flow-perfusion bioreactor system with the incorporation of 3D collagen hydrogel scaffolds to mimic more physiologically representative *in vitro* solid tumors. The sub-saturation of oxygen was created by directing the flow of non-reoxygenated media through subsequent chambers in series. Thus, the oxygen saturation was lowered in a stepwise manner. The verification of sub-saturation oxygen levels was confirmed with optical sensors and the verification of cell culture was determined using cell growth and viability. Further the genetic expression was analyzed using quantitative real time polymerase chain reaction.

1. Background and Significance

The growing field of tissue engineering combines principles of engineering, life sciences, and medicine applied to the understanding of disease mechanisms, the development of new disease treatments, and regenerative medicine. The original goal of tissue engineering focused on repairing and developing whole tissues; however, this goal is still unmet. Key challenges such as tissue vascularization and scale-up for clinical use remain. To address these challenges, the field has expanded into the development of novel platforms for cell growth, nutrient delivery, and functionalized tissues. These platforms aim to provide a biologically relevant growth environment for tissue development or disease modeling. Such platforms include bioreactor systems. Bioreactors aim to improve the cells culturing conditions by providing three-dimensional (3D) culture environments that are reproducible, scalable, and automated. Additionally, bioreactors can be designed to provide platforms closely mimicking *in vivo* tissues states. Currently bioreactors are growing in popularity with stem cell and cancer research.

1.1 Impact of Cancer and Cancer Research

Cancer remains one of the leading causes of death globally with incident rates looking to grow 77% by 2050 [1], [2]. Over the next couple of decades over 35 million new cancer cases will be diagnosed worldwide [1]. Despite the 33% decline in cancer related deaths, it remains the second leading cause of death worldwide [3]. The high diagnosis rate of cancer creates a growing demand for better treatment options in hopes to alleviate the economic and physical burden for patients and their families. Cancer is one of the most expensive medical conditions leading to 71% of patients facing financial hardship within the first two years

following diagnosis [3]. The global economic cost of cancer is expected to reach 25.2 trillion international dollars by 2050 due to the rise in healthcare and drug costs [4], [5]. For example, in the United States, the out-of-pocket cost for insured adult cancer patients averages several thousands of dollars annually potentially reaching tens of thousands for some individuals [6]. The financial burden of cancer treatment can be more expensive depending on the location, type, state, treatment plan, and the patient insurance [7], [8]. Due to the economic burden of cancer treatment, a quarter of cancer survivors reported psychological stress during and post treatment [7]. Further, in response to the economic burden, patients enrolled in copayment assistance programs were found to take less medication than prescribed, only fill half of their prescriptions, did not fill the prescription, or delayed treatment [7]. Thus, a decreased quality of life is experienced by the patients and their families. With the growing number of cancer cases, the significant portion of cancer cases that lack effective treatments, and the growing worldwide economic cost of cancer, there is a high demand for increased cancer research. Cancer research remains one of the most funded research areas globally [9]. However, new treatment options experience exorbitant costs, which leads to limited treatment availability for many patients. For example, chimeric antigen receptor T-cell therapy can be upwards of $500,000 [9]. The complex nature of clinical testing and biopharmaceutical production costs drive the prices of medications upwards in order to maintain a return on investment for companies [10]. Cancer will remain a global societal burden requiring further research in diagnostics, disease characterization, novel therapies, and innovative manufacturing modes. To achieve this, interdisciplinary collaboration and resources are required including biologists, chemists, engineers, among others.

1.2 2D Cell Culture Platforms

Cell culture is a common *in vitro* technique used across many fields, including tissue engineering. Traditional static 2D culture methods such as petri dishes or flasks are the most widely used methods due to their simplicity and low cost. 2D culture models have been beneficial in studies relating to cell migration, adhesion, and scratch assays [11]. However, there are crucial cellular complexities that are overlooked and oversimplified in 2D cultures. Namely, 2D culture environments allow for cell growth in a single monolayer providing an ease of nutrient transport [12]. Monolayer cultures lack native tissue properties such as the presence of oxygen diffusion gradients experienced in 3D tumors. Further, 2D cultured cells are shown to undergo structural and geometric rearrangements of the extracellular matrix (ECM) and cytosol, foreign to cancer cells residing in solid tumors, leading to morphological and expression level changes [13], [14], [15], [16]. These rearrangements lead to a loss of diverse phenotypes, protein expression characteristics, polarity, mRNA splicing, and metabolic profile of cells which ultimately can affect cell function [13], [16], [17]. To address these challenges, 3D *in vitro* culture methods are being developed. Spheroids, organoids, scaffolds, and hydrogels are used for 3D culture [18]. These properties aim to close the gap between *in vitro* studies and *in vivo* clinical trials.

1.2.1 Clinical Drug Efficacy and 2D Cultures

The over-simplified nature of traditional 2D culture methods creates challenges in the transition to clinical trials resulting in limited clinical relevance. One area these limitations are readily evident is drug toxicity testing and efficacy screening. In pre-clinical studies, *in vitro* culture methods are employed to quantify the drug efficacy followed by small animal

models [19], [20], [21]. However, 90% of drugs that pass the preclinical stage will fail in the clinical stage of drug testing [19], [22]. Interestingly, in an analysis of the culture methods used, 66% of respondents reported that 2D cultures were used in preclinical studies [22]. In an additional study of 640 novel therapeutics, 54% failed in late-stage clinical trials primarily due to inadequate efficacy [23]. This suggests the usage of 2D models neglects key components of the structural characteristics of tumors, such as microenvironments, therapeutic uptake of drugs *in vivo*, and native nutrient and signaling molecule gradients. Despite the high rate of failure, the continued dominant usage of 2D models is most likely due to the long history and experience of biomedical scientists using 2D models and their cost-effective nature. However, late-stage failure ultimately results in higher drug development costs due to delays in the progression through clinical trial stages [21]. Thus, researchers are searching for improved culturing models for *in vivo* and clinical studies. 3D culture methods represent an excellent alternative that offers major advantages due to their ability to be designed to closely mimic the physical state of cancer cells in the body.

1.2.2 2D Culture versus 3D Culture and *In Vivo* Models

When selecting a culture method, it is important to consider the ultimate design goals for tissue engineering, namely the expedited transition to *in vivo* studies and their eventual clinical translation to humans. 3D cultures can provide a more accurate platform for pre-clinical modeling to identify early potential problems. 2D cultures are popular due to their relative convenience and have significant limitations as previously described [24].

ECM interactions *in vivo* are complex. A major advantage of 3D culture environments is the incorporation of ECM-like components. The addition of ECM components allows for the

study of migration, morphogenesis, differentiation, and homeostasis [25]. In 3D environments, cells maintain cell-to-cell interactions and tight junctions allowing for further studies of various cell signaling processes [18], [26]. The 3D nature provides cell growth limitations due to diffusional limitations of nutrients. It has been shown that the location of the cell within a 3D environment affects the proliferation rate [27]. Cells located on the periphery experience greater proliferation rates owed to the diffusional limitations of 3D constructs. These limitations also drive cells to undergo metabolic and expression level changes of interior cells [28].

As previously mentioned, the ultimate goal of tissue engineering is clinical translation. Animal models are widely used in tissue engineering to provide reliable information prior to clinical trials. *In vitro* cell cultures models minimize animal testing for drug screenings, which supports the Institutional Animal Care and Use Committee (IACUC) aim of replacement, reduction, and refinement of animal models to reduce unnecessary suffering [29]. Unfortunately, one of the most used animal models in cancer research include nude mice, which lack an immune system. Although heavily used in cancer drug screenings, the efficacy of nude mice is limited, and in the case of immunotherapeutic testing, inaccurate [30], [31]. It is important to note that animal models suffer from species to specific differences [32]. The inability of 2D models to bridge the gap between cell culture and *in vitro* models leads to the development of advanced 3D *in vitro* models [26], [33], [34]. 3D culture environments can replicate *in vivo* atmosphere, with crucial information regarding drug penetration, accumulation, retention and distribution [35]. The development of 3D co-cultures allows better understanding of *in vivo* expected outcomes owed to the presence of complex cellular interactions [36], [37]. For example, in therapeutic testing for colorectal

cancer, the addition of cancer fibroblasts in the culture lead to increased drug resistance [37]. The increased knowledge provided by 3D models minimizes animal suffering and reduces the demand for large numbers of animals by allowing more informed research aims *in vivo*.

1.2.3 Complex *In Vitro* Cultures in Tissue Engineering and Cancer Research

One of the guiding goals of tissue engineering is the ability to grow or regenerate whole 3D tissues without the need for allografting. Therefore, 3D *in vitro* platforms have a crucial role in reaching this goal. It has been noted that traditional culture methods are not meeting the complex demands required for accurate *in vivo* modeling *in vitro*, thus, generating the need for advances in cell culture. For example, human adipose-derived mesenchymal stem cells (MSCs) cultured in spheroid formation indicated stronger antiapoptotic and antioxidative capacities with an increase in paracrine secretion of cytokines for therapeutics as compared to 2D models [38]. Spheroid cultures show great potential for scale-up production of stem cell therapeutics in clinical applications.

In many 3D *in vitro* environments, scaffolds are used to mimic the ECM. The scaffold material can vary depending on the desired tissue type and research goals from synthetic or natural polymers, ceramics, metals, decellularized tissues, and hydrogels among others [39]. Often these models require physical or chemical stimulation, fluid perfusion, or a combination of stimuli to promote viability and cell specialization. In tendon tissue engineering, perfusion flow and tensile stimulation was needed to prevent calcification, or abnormal hardening of the ECM, as generated in MSCs [40]. The lack of calcification indicates the MSCs were differentiating normally and even exhibiting tenogenic phenotype

[40]. Additionally, native tissues consist of different cell types lending to the need for co-cultures for 3D *in vitro* tissue engineered models. In vascular tissue engineering, bovine aortic smooth muscle cells and endothelial cells were co-cultured under pulsating perfusion flow where proliferation increased more than 3-fold with equally distributed collagen and elastin [41]. Using 3D *in vitro* models, the knowledge of natural tissue structure and function can be accomplished. These platforms hold a critical role as the field progresses and transitions into *in vivo* applications.

In vivo models remain the primary model for cancer research. However, *in vitro* models have grown in popularity. Tumors maintain a complex environment with cancer cells, immune cells, fibroblasts, and blood vessels within a complex ECM [42]. 3D tumor models can display *in vivo* like conditions such as chemoresistance, radio-resistance, tumorigenicity, and aggressiveness [43]. The ECM holds a crucial role in tumor progression, metastasis, and response to therapies [44]. These are some of the hallmarks of cancer which require detailed research to better understand their underlying complex interactions. 3D *in vitro* culture methods allow for the incorporation of ECM and cell surface components such as fibronectin and E-cadherin [45], [46]. Cancer cells in 3D tumor models remodel the ECM to aid in metastasis, utilizing matrix metalloproteinases (MMPs) for example [47], [48], [49]. Notably, 3D tumor models *in vitro* have shown a tendency for epithelial-to-mesenchymal transition (EMT), which has been linked to disease progression and metastasis [50], [51]. The physiological relevance of 3D *in vitro* models has expanded into co-cultures to study the interactions of different cell types in the tumor microenvironment (TME). In one study, pancreatic cancer cells were co-cultured with tumor associated fibroblasts in a 3D model to study the effect of cancer fibroblasts on pancreatic cancer cell proliferation rates and

expression of soluble factors [52]. Co-cultures provide a basis for the interconnected components of disease progression in a 3D model.

Solid tumors as 3D constructs are often avascular with nutrient and diffusional gradients prior to the development of leaky vasculature leading to vascular tumors [43]. Oxygen gradients in solid tumors have become a growing focus of research [53]. In solid tumors, a hypoxic core region is often formed due to the diffusional limitations of oxygen. Cancer cells cultured in a hypoxic 3D biomimetic model demonstrated the changes in growth dynamics, with phenotypic features strongly favoring selection of aggressive cells [54]. 3D grown cancer cells cultured in hypoxic environments experienced gene expression and metabolic changes alongside morphological adaptations for diseases progression [55]. For example, hypoxia has been shown to increase EMT resulting in increased potential for metastasis [56]. The hypoxic environment also has been shown to increase drug resistance [57]. The study of nutrient gradients in 3D cancer models allowed for a deeper understanding of cancer mechanisms and therapeutic efficacy.

One of the largest problems facing potential cancer therapies is the poor translation of therapeutic candidates [58]. For example, 5-Fluorouacil, a chemotherapy drug shown to induce apoptosis, downregulated anti-apoptotic genes and reduced cell numbers within 2D models, but merely induced nucleolar stress in xenografts [59]. 3D culture models aim to predict the success of potential cancer therapeutics prior to *in vivo* testing. These platforms allow for controlled analysis of therapeutic mechanisms [60]. As previously mentioned, nude mice, immunocompromised mice, have provided support for cytotoxic drug discovery, however, the field is propelling into inhibitory and immunotherapeutic drugs [61]. TME consists of various immune cells. Thus, utilizing immunocompromised mice models provides

limited efficacy, requiring replacement models. To overcome this gap, 3D co-cultures of cancer and immune cells are being investigated with immunotherapeutic agents [62], [63], [64]. There is a clear demand for models better suited for cancer therapeutic testing prior to clinical trials. Researchers are looking to develop such models to better predict the outcomes of cancer response to new drugs and cytotoxicity [65].

1.3 Significance of Bioreactor Platforms

Bioreactor technology has grown in the field of tissue engineering. Bioreactors are dynamic 3D cell culture systems that allow for highly controlled and reproducible environmental factors. These factors aim to provide a more physiologically relevant environment than traditional static cultures [66], lending to their adoption in many laboratories. In addition to the adaptable cell culture conditions, bioreactor platforms can utilize different biosensors for real-time culture monitoring. The ability to swap sensing modalities proves to be advantageous for analyzing cell cultures or production with higher accuracy [67]. Bioreactor technology aims to provide an ease of clinical translation and further develop 3D culture methods more closely related to *in vivo* conditions.

1.3.1 Current Bioreactor Platforms

There are a variety of bioreactor models used in tissue engineering. The type and conditions of bioreactors are developed to address specific cellular needs. Types of bioreactors include spinner flasks, rotating wall bioreactors, and systems that include compressive stress, tensile strain and flow perfusion [68]. Each modality has unique advantages and disadvantages leading to a wide variety of applications. For example, stirred tank bioreactors are widely used bioreactors in pharmaceutical industry due to their

scalability and application in both bacterial and mammalian cell cultures [69]. Stirred tank bioreactors can reach volumes of 2,000 L. Agitators such as blades or propellers homogenize nutrients, provide uniform distribution of oxygen, and maintain the specified conditions within the culture [69]. However, the agitators can generate harmful shear stress levels. To overcome this, impellors have been modified to provide low-shear conditions for more sensitive cell lines. Specifically, pitched blade impellers and dual-blade impellers generate less turbulence and direct flow to reduce shear stress [69], [70]. Another application of stirred bioreactors is exosome production and CAR T cell therapies, which hold promising futures in cancer therapies [71], [72].

Similarly to stirred bioreactors, spinner flasks are the simplest model of bioreactors. Scaffolds seeded with cells are fixed or suspended in culture media. A magnetic stir bar continuously mixes the media. They can reach volumes of 120 to 8,000 mL with rotational speed of 50-80 rotations per minutes (rpm) [68]. The constant mixture reduces the concentration boundary layer at the construct surface of the scaffold [68]. This is crucial in efforts to provide homogenous nutrient levels at different positions withing the scaffold. Spinner bioreactors have been shown to increase mass transfer due to continuous mixture of the liquid media to improve oxygen and nutrient delivery, as well as waste removal [73]. However, the mass transfer within the scaffold porosity is not enough to maintain equal cell density throughout the scaffold [68], [73]. This limits the cell distribution to primarily the exterior portion of the scaffolds. Additionally, the scaffolds can better mimic transitional and turbulent flow [68]. This can be a disadvantage as the stir bars can cause cell damage or loss of viability due to shear stress [74]. Some research areas utilizing spinner flask bioreactors

are cell suspension [74], cell spheroid formation [73], [74], and cartilage tissue engineering studies [75].

Rotating wall bioreactors are typically cylindrical in shape with free floating scaffolds, where the outer or inner wall is able to maintain constant angular speed and low fluid shear [76]. The rotation provides an upward dynamic force that counters the force of gravity and provides an alternate way to reduce diffusional limitations of nutrients with low shear stress [68], [76]. The result is an induced microgravity environment. This has been shown to prevent cell detachment and sedimentation within the scaffold through the promotion of cell to cell junctions [76], leading to a more homogenous cell density. Example areas of research include stem cell differentiation, cell culture of cartilage, bone, muscle, and skin tissue engineering, and studies in drug testing [76], [77], [78].

Compression and tensile stress bioreactors utilize a motor, a system for providing linear motion for displacements upon a scaffold. Compressive bioreactors are expensive and often require further in house modifications to meet specific research needs [79]. Some of the tensile strain bioreactors resemble compression bioreactors in style and modality. The primary difference is the direction of the force. In tensile bioreactors, the scaffold is clamped within the device so a tensile force can be applied [68]. The Young's Modulus of 3D cell/scaffold constructs increased within tensile bioreactors [68], [80]. Furthermore, cyclic mechanical strain can influence cell behavior, differentiation, and extracellular matrix production [40], [46]. Strain and compressive bioreactors are used to mimic the biomechanical demands of tissues like tendons, ligaments, muscle, and vascular tissues, for example [81].

Bioreactors appear to be aiding in the complexity of *in vitro* models to help bridge the gap between *in vitro* and *in vivo* conditions. To this end, bioreactors provide real-time data of culture conditions through the attachment of modular sensors for nutrient inputs and metabolic outputs. Typically pH, dissolved oxygen (DO), dissolved carbon dioxide, glucose and lactate are standard parameters to be monitored utilizing optical, ultrasonic, electromagnetic, or semiconducting biosensors [83], [84]. Monitoring these conditions are done in the liquid or gas phase, which requires researchers to predict the health of the culture through calculating uptake rates. These are popular modalities due to their non-invasiveness and real-time culture application.

1.3.2 Flow-Perfusion Bioreactors

This thesis focuses on flow-perfusion bioreactors. Flow-perfusion bioreactors consist of a pump, scaffold chamber, media, and tubing. This is due to the ease of use and physical cues provided to the cell culture. The media is forced directly through the interior of the scaffold (if the scaffold is porous) which provides fluid shear stress stimulus [68], [85]. This physical stimulus has been successful in many types of cell cultures, particularly in osteogenic cultures to promote MSC to osteogenic differentiation [86]. Moreover, perfusion bioreactors are being shown to increase vascularization and bone formation from human bone marrow aspirates [87]. Media is easily changed in the reservoir flask and the perfusion rate can generally be controlled on the pump. Additionally, flow-perfusion bioreactors have been shown to have a more homogenous cell distribution and increased cell viability [68]. The fluid flow characteristics have a unique ability to mitigate mass transport limitations found in 3D *in vitro* cultures [88], [89]. Flow perfusion bioreactors have been shown to improve tissue quality through more structurally mature tissues compared to static cultures [90]. The

parameters of flow perfusion bioreactors are controllable and need to be optimized for specific cellular demands. Optimization will provide better mass transfer of nutrients and waste removal while generating shear stress to the cultured cells within the scaffold [68], [90]. These properties are crucial for producing large-scale, viable, and functional tissues.

Flow perfusion bioreactors constitute a unique testing platform compared to 2D or 3D *in vitro* models and microfluidics platforms. Recently, microfluidics developed miniaturized 3D organ-on-a-chip for cancer research models with precise control and high-resolution imaging [91], [92]. However, these platforms lack the ability to accommodate large number of cells and maintain the complex TME [92]. Flow perfusion bioreactors retain the beneficial features of microfluidics, but on a macro scale. A flow-perfusion bioreactor is highly adaptable, allowing for subsequent connection of scaffolds for cell signaling or even utilizing tissue engineered scaffolds of clinical relevance.

Flow perfusion bioreactors have been implemented in pharmaceutical production. Specifically, perfusion bioreactors maintain high cell viability which can lead to greater product production per unit of time [93]. For example, perfusion bioreactors were utilized to produce the SARS-CoV-2 vaccine and yielded 10 times more product than batch fed culture [94]. Further, these systems produce more concentrated products, which in turn can minimize downstream processing cost and complexity [95]. Perfusion bioreactors provide better process control and stability [95], therefore, more consistent product quality and less batch-to-batch variability. These advantages could lower manufacturing costs and return of investment (ROI) for pharmaceutical companies.

1.4 Research Objectives

There were two primary guiding questions, each is represented with an objective below and aim to investigate: 1) “In which ways do sub-saturation of oxygen levels affect the proliferation, oxygen uptake, and genetic modifications of cancer cells in 3D *in vitro* culture with flow-perfusion bioreactor models?” and 2) “How does sub-saturation oxygen levels drive metastatic markers in 3D cancer models?”.

1.4.1 Objective 1

The primary objective of this investigation was to quantify the level of sub-saturation oxygen level, and its cellular effect, induced in a stepwise manner of 3D hydrogel tumor-like environments using flow-perfusion bioreactors. Dissolved oxygen concentrations were measured using phase detection of fluorescent indicators to monitor the sub-saturation oxygen levels for 4 days. The effects of sub-saturation oxygen were evaluated using growth, viability, and oxygen reuptake rates. Further, a mathematical model was applied to empirically estimate the size and depth of the anoxic core region of the scaffolds.

1.4.2 Objective 2

The secondary objective of this investigation was to investigate the effect sub-saturation oxygen levels on metastatic markers for cancer cells. The sub-saturation oxygen level was monitored using phase detection of fluorescent indicators. After the completion of the bioreactor run the gene expression was evaluated using quantitative real time polymerase chain reaction for target genes in oxygen regulation, metastasis, and aggressiveness.

2. Cancer Growth and Metastatic Marker Expression in Sub-Saturation Flow-Perfusion Bioreactor System

Summary

Cancer remains a global malignancy with many challenges in clinical translation due to inaccurate *in vitro* models. Currently, *in vitro* models rely heavily on 2D monolayer cultures which lack the physiological relevance of 3D cultures. Additionally, studies using 3D cell culture techniques lack potentially critical components of the tumor microenvironment such as fluid flow. Microfluidics have grown in popularity for 3D cultures with fluid flow. However, microfluidics lack the scale needed to accurately mimic solid tumor pathophysiology. This study proposes the use of a modified flow-perfusion bioreactor with 3D collagen hydrogel scaffolds as a solid tumor microenvironment that more closely resembles *in vivo* characteristics. Bioreactor chambers were connected in series with oxygen impermeable tubing preventing bulk media reoxygenation between chambers to generate a stepwise induction of artificial sub-saturation levels of oxygen. This configuration creates variable oxygen saturation levels, which is a crucial variable in the treatment and disease progression of solid tumors. The bioreactor utilized previously optimized optical sensors to confirm drop in oxygen saturation of media. From these measurements, the oxygen uptake per scaffold and per chamber was determined. Cell proliferation and viability were assessed to determine the effect of sub-saturation oxygen levels, which confirmed the increase in hypoxic core region volume and decreased distance to this region for downstream chambers.

These estimations were calculated using a modified spheroid hypoxia model and the empirically measured data for the collagen hydrogels and epithelial mouse tumor 6 (EMT6) cell line. Finally, gene expression of crucial hypoxia regulatory genes and downstream targets for disease progression and aggressiveness were monitored. The results confirmed sub-saturation oxygen level with cellular response of downstream chambers.

2.1 Introduction

Oxygen has a vital role in cell survival, growth, differentiation, and general success of the tissue construct. Oxygen is used to maintain cellular homeostasis and generate adenosine triphosphate (ATP) using aerobic metabolism to maintain basic cellular functions. However, under oxidative stress, cells can experience acidosis due to the decrease in pH from lactic acid build up during anaerobic metabolism [96]. Additionally, cells experiencing oxidative stress release reactive oxygen species (ROS) and microvesicles that carry signaling capacity and can potentially induce apoptosis to neighboring cells, among other effects [97], [98]. Oxygen availability greatly dictates the cell viability and survival of many differentiated cell types. Unlike terminally differentiated cells, oxygen often mediates cell differentiation by promoting self-renewal, inhibiting certain differentiation pathways, and affecting the gene expression in cell fate decisions [99]. Some studies indicate hypoxia results in maintenance of stem cell potency and increased proliferation rates, while other studies have indicated even a small shift in oxygen tension can induce differentiation [100], [101]. For example, hypoxia has been shown to drive adult stem cell differentiation into chondrocytes [100].

One of the greatest challenges in tissue engineering is vascularization. Oxygen is supplied to tissues through passive diffusion, which generates a decreasing oxygen gradient

from the tissue periphery towards the tissue core. In native tissues, the diffusional limit of oxygen is approximately 100 to 200 μm [102]. Therefore, the size of tissue constructs *in vitro* is limited. In efforts to increase vascularization in 3D *in vitro* constructs, the addition of angiogenic growth factors, such as vascular endothelial growth factor (VEGF), and oxygen-releasing biomaterials have been implemented for increasing *in vitro* vascularization and control of oxygen-release kinetics [103], [104]. These methodologies overlook the dynamic environment of native tissues constructs. As previously mentioned, microfluidics provide a controlled dynamic culture environment for oxygen supply or delivery of growth factors for increased tissue construct viability [105]. However, microfluidics focuses on small scale cultures, rather than larger constructs. Perfusion bioreactors provide a large scale, dynamic culture environment to overcome the diffusional limitation of oxygen *in vitro.* Within these systems, various oxygen sensors have been implemented for real-time culture monitoring. Optical sensors are becoming increasingly popular due to their non-invasive nature, quick response time, ease of use, and versatility in bioreactor size [83].

2.1.1 Pathophysiology and Solid Tumor Microenvironment

Blood supply of normal tissues is maintained through highly ordered and efficient vascular networks. These blood vessels are metabolically regulated by pro-angiogenic and anti-angiogenic factors and lymphatic vessels to result in evenly distributed mature vessels for proper oxygen and nutrient diffusion [106]. Solid tumors require similar nutrient and waste removal systems as normal tissues. However, the aggressive tumor growth and the pro-angiogenic factors released leads to leaky and disorganized blood vessels networks [106], [107]. Tumor vasculatures are inconsistent in diameter, unevenly shaped, and have increased permeability which led to decreased nutrients and waste removal via the lymphatic system

[106], [107]. As such, cancer cells within the tumor are nutrient and oxygen starved but are largely considered to be viable. The increased vessel permeability causes increased interstitial fluid pressure within the tumor [108]. This increase in interstitial fluid pressure has been associated with lower survival rates and provides challenges in drug delivery [109], [110]. The environmental conditions within the tumor environment are harsh, which leads to genetic abnormalities and reprogramming of the immune system for survival.

The tumor microenvironment is complex, consisting of many cell types not limited to only cancer cells and cancer stem cells. Figure 2.1 highlights the key cell types and vascularization of solid tumors. A central cell type that shapes the tumor microenvironment are immune cells. The most prominent immune cells are macrophages, natural killer (NK) cells, and lymphocytes [42]. The specific interaction between immune cells and cancer cells is actively being investigated; however, it is largely understood that these immune cells are critical to the survival of solid tumors [42]. Specifically, M2 tumor-associated macrophages (TAMs) are predominately present within the TME [111]. The M2 macrophages maintain anti-inflammatory and tumorigenic properties. M2 TAMs contribute to the immunosuppressive nature of cancer cells [112]. TAMs have been noted to promote invasion and metastasis by releasing degrading enzymes such as serine proteases, metalloproteinases, and cathepsins [111], [113]. These cause tumors cells to detach and generate distant metastasis through the breakdown of collagen. Further, TAMs can release factors such as IL-8, CCL8, and VEGF to aid in angiogenesis [111], [112]. T lymphocytes also aid in disease progression. Regulatory CD4+ T-cells can aid in immune evasion by silencing CD8+ T cells through immune checkpoint molecules such as PD-1 and cytotoxic T-lymphocyte-associated protein 4 (CLTA4) [114].

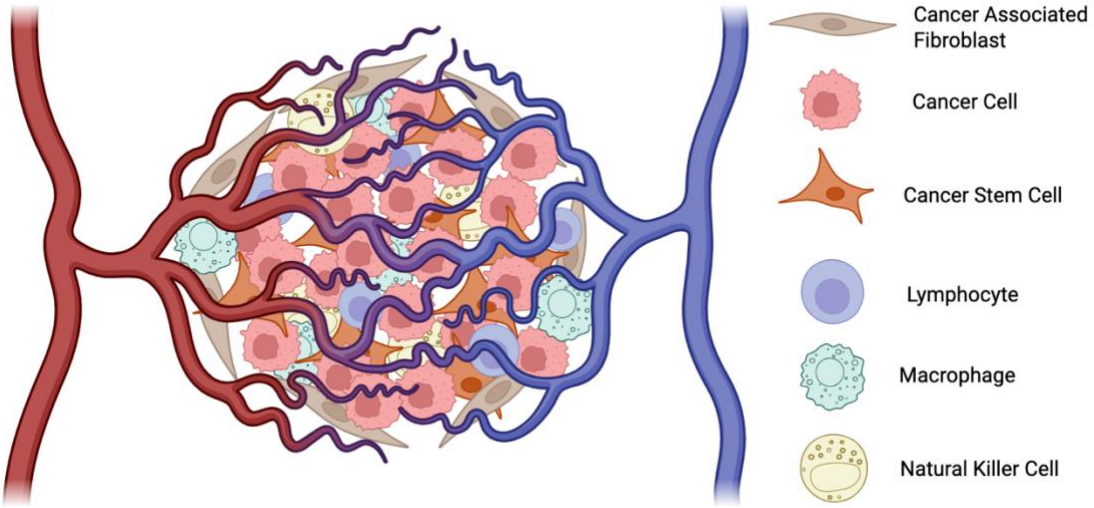


Figure 2.1: Solid Tumor Microenvironment

Illustration of the solid tumor microenvironment consisting of cancer cells, cancer stem cells, and various immune cells to represent the various phenotypes present. Abnormal vascularization is depicted due to rapid cancer growth. Image generated in BioRender.

Cancer associated fibroblasts (CAFs) are also present within the solid tumor microenvironment. In healthy tissues fibroblasts are associated with ECM remodeling and synthesis. CAFs support tumor growth and viability through the secretion of growth factors, inflammatory ligands, and ECM proteins that promote growth, and tumor resistance, and immune exclusion [115]. CAFs can provide a physical barrier for the tumor cells leading to denser tissues and an increased difficulty in therapeutic penetration [115]. Matrix metalloproteinases (MMPs) are secreted to promote the invasion of cancer cells [116]. CAFs can polarize macrophages to the M2 subtype through the secretion of C-X-C motif chemokine 12 (CXCL 12) [117]. A wide variety of cell types actively support the tumor microenvironment through complex interactions.

Another crucial component of tumor pathophysiology is glycolytic metabolism. Under normal conditions with stable, sufficient oxygen supply, cells undergo aerobic oxidation where glucose oxidizes to water and carbon dioxide. However, in reduced oxygen tensions, cells undergo anaerobic oxidation where glucose oxidizes to pyruvate, which eventually becomes lactate, or lactic acid. Using anaerobic glycolysis, the production of lactate occurs 10-100 times faster than the complete oxidation of glucose [118]. Due to the increased lactic acid production, the tumor microenvironment experiences an acidic pH [119]. Most cancer cells have been observed to altered their metabolic profile where glucose is oxidized through glycolysis even in the presence of oxygen, which is known as the Warburg Effect [118]. Tumor suppressor gene expression and overexpression of oncogenes have a crucial role in the Warburg effect. Of the regulatory genes for glycolysis, Hypoxia Inducible Factor 1α (HIF-1α) and Phosphatidylinositol-3-kinase (P13K)/Akt/mammalian target of rapamycin (mTOR) pathways are crucial in the Warburg effect [120], [121]. P13K/Akt regulates mTOR, which amplifies the Warburg effect by stimulating normoxic upregulation of HIF-1 [120]. Additionally, the deactivation of threonine kinase B1 (LKB1), AMP-activated protein kinase (AMPK), and cMYC transcription factor are key metabolic deregulators. C-MYC interacts with HIF-1 to further the Warburg effect by increasing the expression of glycolytic enzymes [120].

Cancer cells serve as glucose traps due to the decrease in pyruvate kinase (PK) enzyme, which converts phosphoenolpyruvate (PEP) to pyruvate [122]. One crucial component in cancer metabolism is the upregulation of pyruvate kinase isoform M2 (PKM2), a cytosol glycolytic enzyme with low catabolic activity that interacts with the Hypoxia Inducible Factor 1α (HIF1α) subunit, after the activation of HIF-1 and P13K pathways [121], [122].

Thus, a positive feedback loop for anaerobic glycolysis is created enhancing the Warburg effect. Further, HIF-1α upregulated pyruvate dehydrogenase kinase isoform 1 (PDK1) to enhance the Warburg effect [119]. PDK1 blocks the pyruvate from entering the mitochondria and lactate dehydrogenase A (LDH-A) from catalyzing pyruvate into lactate in the cytosol [122], [123]. Lastly, tumor suppressor gene p53 regulates glucose metabolism by inhibiting glucose transporters [124].

Cancer is marked by cell behavior, genetic adaptations, metabolic activity, immune evasion, and the ability to metastasize. As discusses previously, the tumor microenvironment aids in the metastasis of cancer cells in a variety of ways, however, another key pathway for metastasis is epithelial-mesenchymal transition (EMT) dedifferentiation [125]. EMT-dedifferentiation is a tightly regulated process of multiple transcription factors, epigenetic modifications, and noncoding RNA-mediated regulations [126]. Crucial signaling pathways for EMT-dedifferentiation include ZEB1, Notch, and Snail1 [127]. In these processes, specialized epithelial cells lose differentiated characteristics to revert to a less connected, stem-like state for ease of migration.

2.1.2 Hypoxia in Cancer

Hypoxia is present in nearly 90% of solid tumors and has become a hallmark of cancer gene expression of cell proliferation, migration, invasion, and angiogenesis [128]. Therefore, there has been an increase in hypoxia related solid tumor pathophysiology research. Hypoxia is defined as a reduction in oxygen pressure between 0-20 mmHg, which can occur due to an imbalance of oxygen supply and consumption [129]. Hypoxia Inducible Factors (HIFs) are transcriptional factors to regulate and respond to low oxygen levels. There are three primary

HIF isoforms: HIF-1, HIF-2, and HIF-3 which all are heterodimers containing a constitutively expressed β subunit and an oxygen regulated α subunit. Both HIF-α and HIF-β have basic helix-loop-helix motifs for DNA binding and subunit dimerization [130]. However, under normoxic conditions, the HIF-α subunit is continuously synthesized and regulated through hydroxylation by proline-hydroxylase-2 (PHD-2) leading to proteasomal degradation of the α subunit [130], [131]. Under reduced oxygen conditions, HIF-α stabilizes as proline hydroxylase (PHD) hydroxylation is suppressed and HIF-α degradation is reduced [131]. HIF-α translocates to the nucleus where it dimerizes with HIF-β and binds to the hypoxia response elements (HRE) promoter or enhancer of target gene sequences [131], [132]. HIF-1 and HIF-2 have been more extensively studied, and target similar genes, while research on HIF-3 remains limited. Evidence suggests HIF-1 is primarily involved in acute adaptation to hypoxia, where HIF-2 has greater prominence in prolonged hypoxia for vascular network maturation [133]. Further evidence suggests HIF-1α stabilizes the hypoxic core of solid tumors during rapid expansion and poor vascularization [132].

In cancer, HIFs have a role in immunosuppression. HIF-1α promotes various immune suppressive pathways, secrete immune suppressive cytokines such as transforming growth factor beta (TGF-β) and interleukin 10 (IL-10) [134]. These cytokines interfere with cluster of differentiation (CD) mediated priming of CD8+ T cell and natural killer (NK) cell function, while promoting the immunosuppressive activity of myeloid-derived suppressor cells (MDSCs) and T regulatory cells (Tregs) [134], [135]. The inhibition of T cell priming and activity hinders T cell ability to target and kill tumor cells. HIF-1α suppresses cytotoxic T lymphocytes (CTLs) and NK cell infiltration in tumors due to decreased major histocompatibility complex 1 (MHC-1) and Fas on the surface [134], [135]. Moreover, HIF-

1α upregulates immune check points such as cytotoxic T-lymphocyte- associated antigen-4 (CLTA-4) and programmed cell death ligand 1 (PD-L1) [136]. The upregulation of these immune checkpoints decreases the T cell activity. The role of HIFs in immunosuppression aid tumor progression.

Cancer cell metabolism is another aspect affected by HIFs. HIF-1α is understood to play a key role in several steps of the Warburg effect. Namely, HIF-1α stimulates the uptake of glucose to compensate for the metabolic inefficiencies of glycolysis by upregulating glucose membrane transporters such as GLUT1 and GLUT3 [132], [137]. Additionally, HIF-1α upregulates glycolytic enzymes and inhibits mitochondrial respiration through the activation of pyruvate dehydrogenase kinase (PDK) [137]. PDK in turn phosphorylates and inactivates pyruvate dehydrogenase (PDH) and shunts pyruvate from the mitochondria [137], [138]. Therefore, there is a reduction of mitochondrial ROS, and a decrease in oxidative stress for the cancer cells [139]. With glycolysis being a primary method for metabolism, lactic acid is a byproduct that can accumulate in the cells and decrease the internal pH. HIF-1α can buffer the pH by upregulating carbonic anhydrase 9 and 12 to catalyze hydration of carbon dioxide into bicarbonate [132]. Further, HIF-1α increases transcription of lactate transporters in response to lactic acidosis [139], [140]. HIFs act as transcriptional regulators for the genes involved in cancer metabolism to support cancer cell survival in hypoxic conditions.

HIFs have been suggested to influence drug resistance and cancer drug efficacy. HIFs promote chemoresistance by enhancing the expression of ATP Binding Cassette (ABC) transporters, which are responsible for the efflux of chemotherapeutic agents [141]. Specifically, HIF-1 activates multidrug resistance 1 (MDR1), a gene that encodes for

membrane-resident P-glycoprotein (P-gp) which has been shown to decrease intracellular concentration of chemotherapeutics [142]. ABC expression is HIF-1 and HIF-2 dependently induced under hypoxic conditions [141]. Additionally, HIF-1 also has been shown to upregulate the expression of apoptosis proteins to promote cell viability and drug resistance. Pro-apoptotic and anti-apoptotic factors have been identified as HIF-1 regulated, although the exact mechanism remains largely unknown [142]. However, HIF-1 and HIF-2 mediated suppression of p53, a pathway crucial to chemotherapy-induced apoptosis, activation has been reported [142], [143]. The role of HIFs and hypoxia are being investigated for both chemotherapeutic resistance as well as development of therapeutics to target HIFs.

The complex nature of hypoxia in cancer progression and treatment efficacy requires novel, accurate *in vitro* culture method for more accurate characterization and efficacy studies. This study modified a flow-perfusion bioreactor to model 3D *in vivo* tumors creating a stepwise decrease of oxygen tension in collagen hydrogels. Sub-saturation oxygen tensions were monitored using optical oxygen sensors. Genetic expression hypoxia genes and genes in disease progression and metastasis were analyzed using quantitative real time polymerase chain reaction to characterize cancer cells post culture in perfusion-flow, sub-saturation oxygen tensions. Further, empirical analysis was conducted to estimate the size of the hypoxic core region in a 3D hydrogel scaffold. On a larger scale, monitoring the oxygen tension and genetic expression of cancer cells cultured in flow-perfusion bioreactors were analyzed for insights into larger scaffold viability for tissue engineering applications.

2.2 Methods

2.2.1 Cell Culture

The selected cell line used in this experiment was EMT6, a murine epithelial breast cancer line. All cells were cultured in T75 culture flasks and flow perfusion bioreactors with Waymouth Media (Gibco) supplemented with 15% fetal bovine serum (FBS) (Life Technologies) and 1% antibiotic/antimycotic (Life Technologies) in an incubator set to 37°C and 5% CO_2. Prior to seeding cells in a scaffold for culture in the bioreactor, the EMT6 cells were expanded in a T75 culture flask until 85% confluent. The cells were lifted using 0.05% Trypsin-EDTA (Sigma-Aldrich) and neutralized using supplemented Waymouth Media for centrifugation. One-half mL of cell solution was retained in a sterile microcentrifuge tube for cell quantification as described in section 2.2.11 prior to centrifugation. Cells were centrifuged at 800 relative centrifugal force (RCF) for 5 minutes and the supernatant was discarded. The remaining cell pellet was resuspended in new supplemented Waymouth media at the desired concentration for scaffold seeding.

2.2.2 3D-Printed Poly-L-Lactic Acid Cassette Holder Production

A custom designed 3D-printed PLLA mesh holder to support collagen hydrogels in the bioreactor chambers was previously designed in Autodesk Fusion360 by Bryant et al. [144]. The purpose of the PLLA holder was to elevate the collagen hydrogels seeded with EMT6 cells above the bioreactor fluid exit, provide space between the cassette and chamber wall, and provide structural support to the hydrogel during perfusion flow, which led to unobstructed media flow around and through the hydrogel for increased nutrient diffusion. Figure 2.1 contains the 3D rendering of the PLLA holder and assembly prior to placement in

the bioreactor chamber. The holder was printed using the custom extruded PLLA filament on Creality Ender V2 Neo 3D printer.

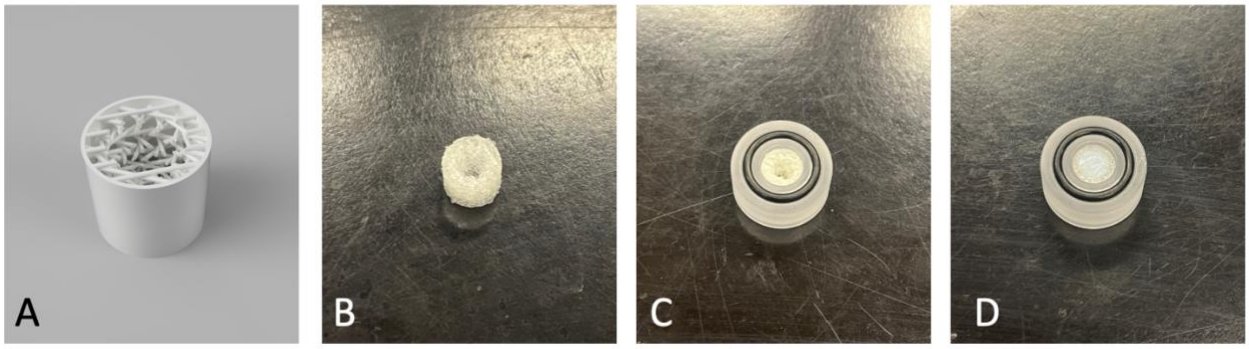


Figure 2.2:PLLA Hydrogel Holder

Illustration of the PLLA hydrogel holder design and assembly into the cassette. A) 3D design of the holder in AutoDesk Fusion 360, image used with permission of author at the following reference [144]. B) 3D printed mesh holder printed on a Creality Ender 3 V2 Neo printer. C) Mesh holder inserted into the cassette holder for placement into a bioreactor chamber. D) Collagen hydrogel inserted into the PLLA mesh holder insider the cassette.

2.2.3 Oxygen Sensor Assembly

During the bioreactor runs, the oxygen saturation in the media was monitored. To do this, RedEye Oxygen Sensing Patches (Ocean Optics) were placed inside an oxygen sensing module (OxyMod) developed by Simmons et al. [145]. Briefly, the main body of the oxygen sensor consisted of a square glass tube where the oxygen sensing patch was placed inside. The glass tube was then placed inside a custom designed 3D-printed housing to serve as a guide for the probe. Two barbed tubing fittings were then attached to the ends of the sensor and sealed with marine epoxy. Assembled OxyMod is shown in Figure 2.3 below.



Figure 2.3:OxyMod Sensor Assembly

Oxygen sensor design by Simmons et al. for integration into the perfusion bioreactor system. PLLA 3D printed casing with a probe guide to block excess light during real time oxygen saturation measurements.

2.2.4 Bioreactor Assembly

The bioreactor consisted of a metal stand to hold an acrylic plate with 6 individual chambers. Each chamber held an individual collagen hydrogel scaffold, PLLA mesh scaffold to support the hydrogel, and cassette to house the scaffolds in the chamber. The chambers were sealed with a polymer-based screw top. The chambers were connected using silicon tubing (either oxygen permeable or oxygen impermeable). Figure 2.4 and 2.5 contains a schematic of the bioreactor system and a cross-sectional view of one bioreactor chamber, respectively. Fluid flow was achieved using a peristaltic pump with a flow rate of 150 μL/min and at least one media vessel of bulk media. The media was circulated through the bioreactor chambers entering at the chamber top, flowing through the chamber and collagen hydrogel, and exiting through chamber bottom. Each run used 70 mL of supplemented media. The oxygen parameters were adjusted based on the type of silicon tubing (oxygen permeable or oxygen impermeable) and the tubing configuration (series verse parallel).

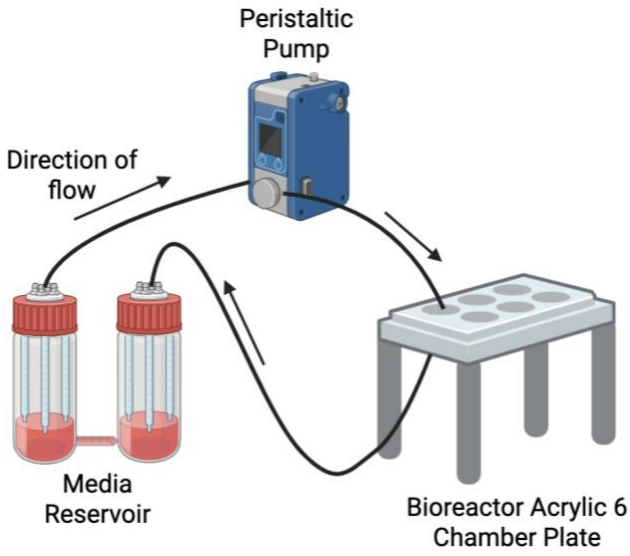


Figure 2.4: General Bioreactor Schematic

The novel flow-perfusion bioreactor used in this investigation consists of a peristaltic pump, a media reservoir, and an acrylic 6 chambered bioreactor all connected by tubing. All tubing and chamber components are fitted to avoid leaks throughout during perfusion. Image created using BioRender.

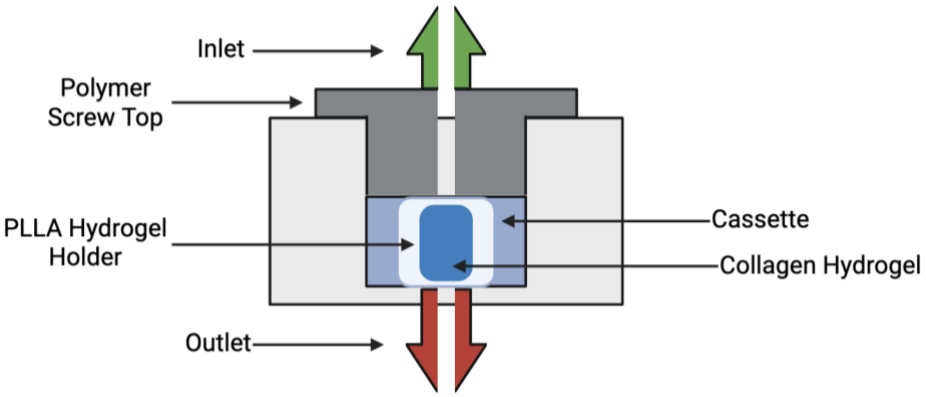


Figure 2.5: Cross Sectional View of One Bioreactor Chamber

Fitted tubing covers the inlet and outlet barbs of the chamber. Media is perfused through the polymer screw top, and chamber containing the cassette, PLLA hydrogel holder, and collagen hydrogel before exiting the outlet. Image created using BioRender.

By using the series configuration, the scaffolds were pushed into a simulated decrease in oxygen conditions, which is designed to mimic the larger scaffolds required for tissue engineering. Figure 2.6 outlines the series configuration used in this experiment. For the series configuration, the chambers were connected by oxygen impermeable tubing where the outlet of an upstream chamber fed directly into the inlet of downstream chamber. This prevented reoxygenation of the media and generated a stepwise decrease in saturated oxygen concentration of the media as the chamber number increases. A long oxygen permeable tube connected the inlet of chamber 1 to the bulk media vessel, ensuring the media leading into chamber 1 was reoxygenated. Due to the long tubing length, it is assumed the oxygen saturation in the media is 100% at the entrance of Chamber 1. One media vessel is used in the series configuration, where oxygen permeable tubing was connected from the media reservoir to Chamber 1. After the media is circulated through all 6 chambers, the media exiting Chamber 6 is return to the media reservoir. To monitor the oxygen saturation within the bioreactor, three oxygen sensors were used. The sensors were placed after Chamber 1, Chamber 5, and Chamber 6.

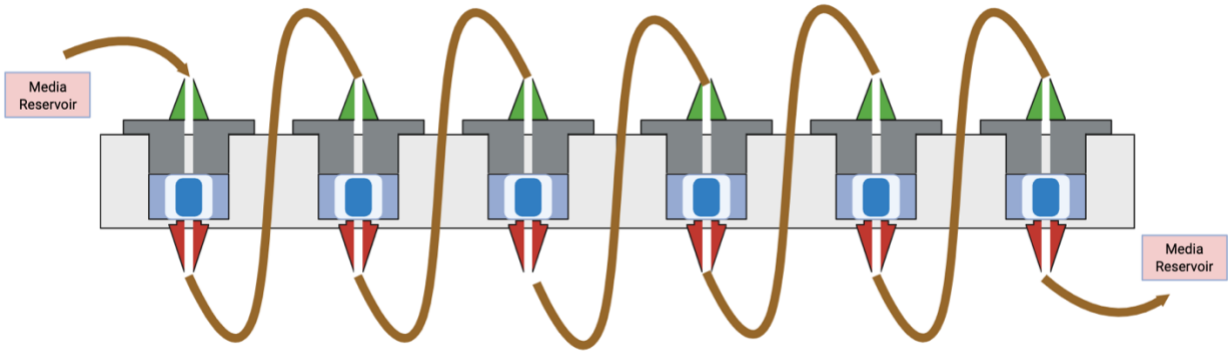


Figure 2.6: Series Bioreactor Configuration

Diagram of the 6 bioreactor chambers in series to induce a stepwise decrease in oxygen saturation of the media. The outlet of each chamber is pumped into the inlet of the next chamber with oxygen impermeable tubing beginning after chamber 1. Specifically, the media exiting chamber 1 enters to inlet of chamber 2, the media exiting chamber 2 enters the inlet of chamber 3, the media exiting chamber 3 feeds into the inlet of chamber 4, and the exiting media of chamber 4 feeds the inlet of chamber 6, and the exiting media from chamber 6 is returned to the media reservoir. Long oxygen permeable tubing is connected to the inlet of chamber 1. Therefore, the oxygen concentration of the bulk media is reduced at the chamber number increases due to cellular consumption of oxygen.

The purpose of parallel configuration was to mimic 3D cultures under standard growth conditions of 100% oxygen saturation with perfusion flow of nutrients. Figure 2.7 outlines the configuration of the parallel variation of the bioreactor set-up. For the parallel configuration, each chamber was individually connected to the media reservoir (i.e. the media recycled to the media reservoir after cycling through one individual scaffold). The media reservoir consisted of two media vessels connected by oxygen permeable tubing. Each chamber was connected to one media vessel and after flowing through the individual chamber, the media was returned to the second media vessel. All oxygen permeable connective tubing was used. With all oxygen permeable tubing used, the oxygen saturation

level was assumed to be 100% for all chambers. An oxygen sensor will be placed at the exit of each chamber in this configuration to monitor the oxygen saturation.

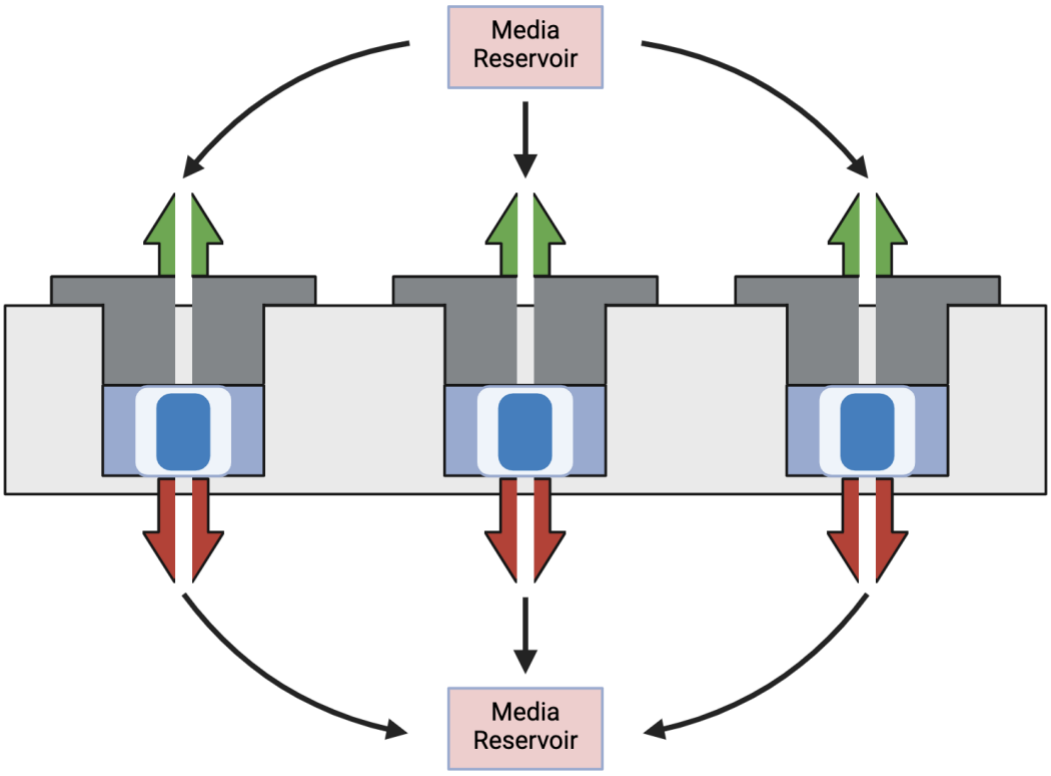


Figure 2.7: Parallel Bioreactor Configuration

Diagram of 3 out of the 6 chambers of the bioreactor where media is pumped parallelly, so the media flows from the media vessel to one chamber and is returned to the media vessel. All oxygen permeable tubing was used. This variation simulated normoxic 3D culture conditions with fully oxygen saturated media.

Prior to the assembly of the bioreactor, all tubing and polymer components were sterilized using ethylene oxide (Anprolene AN75, Andersen Sterilizers). Gas sterilized components were run in a 12-hour cycle and stored in a fume hood for 3 days to outgas excess ethylene oxide. All other autoclavable parts were autoclaved the same day as bioreactor assembly. The bioreactor was assembled under sterile, aseptic conditions in a

biosafety cabinet prior to transferring seeded collagen hydrogels into the bioreactor. The bioreactor was placed in the incubator and media was allowed to flow throughout the system to purge air and allow time for the media to equilibrate to culture conditions. Media was circulated at 1000 μL/min for 4 hours before cell seeding to allow for equilibration and prime the chamber with media for the cell-seeded hydrogels.

2.2.5 Hydrogel Formation

To prepare the seeded hydrogel scaffolds, EMT6 cells were lifted using 0.05% Trypsin-EDTA (Sigma-Aldrich) and collected in a pellet through centrifugation at 1100 RCF for 5 minutes. Prior to centrifugation, 0.5 mL of cell suspension is placed into a microcentrifuge tube for cellular quantification as described in section 2.2.11. The supernatant was discarded, and the cells were resuspended in new media to reach a concentration ten times the final desired seeding concentration. The collagen hydrogels were prepared using RatCol Rat Tail Type I Collagen Hydrogel (Advanced Biomatrix). The collagen hydrogel and the provided neutralizing solution were mixed thoroughly following the manufacturer's instructions of a 1:9 ratio, resulting in a collagen concentration of 4 mg/mL. By mixing the collagen with the neutralizing solution before adding cell solution, ensured the acidic nature of the collagen was a neutral pH. Therefore, the cells were not subjected to an acidic environment. The high collagen concentration provided resistance to damage from fluid flow within the bioreactor. To shape the hydrogels, 0.4 mL neutralized collagen solution was thoroughly mixed with 0.1 mL cell suspension for each chamber. This ensured the cells were evenly distributed throughout the hydrogel and avoided spheroid formation. Each chamber was seeded at 1.5 million cells. The collagen hydrogel cell solution was pipetted into a well of a 96 well plate. This was repeated 6 times, one gel for each of the 6 chambers. Next, the 96 well plate was

incubated at 37°C and 5% CO_2 for 1 hour, or until firm. Once firm, the hydrogels were transferred into the bioreactor and placed inside the PLLA mesh scaffold using tweezers. The bioreactor was sealed and placed back in the incubator. The flow rate was set to 150 μL/min. Each bioreactor run lasted 4 days with no media change.

2.2.6 Oxygen Data Collection

The oxygen sensors utilized RedEye oxygen sensing patches (Ocean Optics). The patches contain two fluorescent molecules: ruthenium and Pt-porphyrin. A blue fiber optic probe was used to pulse blue light at 450 nm to excite the fluorophores material and capture the emitted light. The fluorescent emission is directly related to the oxygen saturation of the media through the Stern-Volmer equation (Equation 2.1). The oxygen saturation levels ranged from 0% to 100% where the maximum oxygen saturation was given under standard conditions (37°C, 5% CO_2). The partial pressure of oxygen at 100% saturation was calculated using Henry's Law (Equation 2.2) under conditions of 1 atm, 95% relative humidity, 5% CO_2, and 21% O_2, where the constant (K) was computed using the Van't Hoff equation (Equation 2.3) to account for the incubator temperature of 37°C of 1.04 mmol/L/atm [146]. The concentration of dissolved oxygen was assumed to be 0 at 0% saturation. The concentration values of 0% and 100% saturation created a linear equation relating the oxygen saturation to the dissolved oxygen concentration (Equation 2.4).

$$\frac{F_0}{F} = \frac{\tau_0}{\tau} = 1 + k_q * \tau_0 * [O_2] = 1 + K_{SV} * [O_2] \quad \textbf{Equation 2.1}$$

$$C = K(P) \quad \textbf{Equation 2.2}$$

$$\frac{d}{dT}\ln(K) = \frac{\Delta H}{RT^2} \quad \textbf{Equation 2.3}$$

$$C = 0.00195(Saturation\ Oxygen)\ \textbf{Equation 2.4}$$

Where: F_0 = fluorescent intensity in absence of O_2

F = fluorescent intensity in presence of O_2

τ_0 = fluorescent decay time in absence of O_2

τ = fluorescent decay time in presence of O_2

k_q = bimolecular quenching constant

K_{SV} = Stern-Volmer constant for static decay

$[O_2]$ = concentration of molecular oxygen present at fluorophore

R = ideal gas constant

ΔH = standard enthalpy change

K = equilibrium constant

T = Temperature

C = concentration of dissolved oxygen gas

P = partial pressure of oxygen

Oxygen sensors were placed at the exit of chamber 1, 5 and 6 for the series configuration and placed at the exit of every chamber in the parallel configuration. The placement of oxygen sensors after chamber 1, 5 and 6 in the series configuration was decided as the

sensors can occasionally trap small oxygen bubbles allowing for reoxygenation of media. Having the sensors spread apart minimizes potential reoxygenation of the media downstream. Additionally, the placement measures the oxygen saturation at the beginning and end of the bioreactor system, which can be representative of oxygen levels throughout a larger scaffold. The oxygen saturation of media after chamber 1 represents the oxygen saturation near the surface of a scaffold and the oxygen saturation after chamber 6 represents the oxygen saturation at the end of a long scaffold or alternatively at a point simulated deep within a scaffold. Using the fiber optic probe and the NeoFox Viewer software, the real time saturation percent values were recorded every 10 seconds for one minute once a day for the duration of the 4-day bioreactor run. These 6 readings were averaged to minimize noise. The oxygen concentration was calculated using the developed linear equation outlined in Equation 2.4.

2.2.7 Oxygen Sensor Calibration

Before each bioreactor run, the oxygen sensors were calibrated. Prior to gas sterilization, the oxygen sensors were calibrated to 100% saturation and 0% saturation. The bioreactor was assembled and deionized water was used in place of media. For the 100% calibration, the bioreactor was placed inside the incubator with all oxygen permeable tubing. The flow rate was set to 150 μL/min for 12 hours. Following the 12 hours, the τ, the fluorescent time constant, values for each sensor were recorded as described in section 2.2.7. For the 0% calibration, the bioreactor was assembled with all oxygen impermeable tubing. The media vessel was then filled with deionized water. A diffusing stone was attached to a nitrogen air tank with oxygen impermeable tubing and placed into the media vessel. The flow rate was set to 1000 μL/min and ran for 4 hours. This method purges the oxygen from the system. After

the 4 hours, the τ values for each sensor were recorded. The measured τ values provide sensor specific calibrations that are applied to the two-point calibration curve in the NeoFox Viewer software. Following the sterilization and assembly of the bioreactor with supplemented media, the oxygen sensors were calibrated to the 100% oxygen saturation of the media. 70 mL of media was added to the media vessel and the bioreactor was placed in the incubator for 4 hours with a flow rate of 1000 μL/min. Following this equilibrium period, the τ values from the deionized water 0% and 100% were applied to the NeoFox Viewer two-point calibration. The τ value of the media was recorded. This τ value replaced the 100% oxygen calibration of deionized water and was applied for each oxygen reading post cell seeding.

2.2.8 Oxygen Uptake Calculations

The oxygen uptake rate (OUR) per scaffold was calculated using Equation 2.5 described by Felder et al [147].

$$OUR_{scaffold} = \left(C_{O_2,in} - C_{O_2,out}\right) * v \quad \textbf{Equation 2.5}$$

In the equation, $C_{o_2,in}$ is the concentration of oxygen at the entrance of the chamber and $C_{o_2,out}$ is the concentration of oxygen at the exit of the chamber. The concentration was calculated using the linear relation model discussed in section 2.2.7 with both values being measured in μmol/L. It is important to note, the $C_{o_2,in}$ for chamber 6 was calculated from the average oxygen saturation measured after chamber 5. Lastly, v is the volumetric flow rate in L/hr. The OUR per cell can be calculated using Equation 2.6, where N_{cell} is the total number of cells in the scaffold.

$$OUR_{cell} = \frac{OUR_{scaffold}}{N_{cell}} \quad \textbf{Equation 2.6}$$

2.2.9 Hydrogel Dimension Measurement

To measure the dimensions of the collagen hydrogel scaffolds, post 4-day culture within the bioreactor, an image was taken with a ruler to provide a known scale length. The image was loaded into ImageJ Software where the length, width, and height were calculated. Since collagen hydrogels are known to compact during cell culture, the percent change in volume of each scaffold was calculated based on the original 0.5 mL volume during cell seeding. The volume of hydrogels was calculated using Equation 2.7 for an elliptical cylinder. In the equation V is the volume, a and b are radii, and h is the height.

$$V = \pi abh \quad \textbf{Equation 2.7}$$

2.2.10 Estimation of Anoxic Core Region

Cultures grown in 3D can experience anoxic or hypoxic core regions due to diffusional limitations. A mathematical model is applied to estimate the size of such regions within the collagen hydrogels similarly to Bryant et al. [144]. This model was adapted from Grimes et al. and modified empirically with measured values for the diffusion of oxygen through collagen hydrogels by Colom et al. [148], [149]. As described by Grimes et al., the model was derived initially from a diffusion equation and consumption factor in Equation 2.8.

$$\frac{\partial C}{\partial t} = D\nabla^2 C - a(r) \quad \textbf{Equation 2.8}$$

In this equation, D is the diffusion constant of the tissue which is 2.0 x 10^{-9} m^2/s, C is the volume of oxygen per unit mass, and $a(r)$ is the oxygen consumption rate at point r [148].

Several key assumptions were made. First, the oxygen is supplied at steady- state; second, the model considers a spheroid shape where the cells comprise the entire sphere; and third *a(r)* is constant throughout the model. The equation can be rewritten using spherical Laplacian coordinates to create equation 2.9.

$$a(r) = \frac{D}{r^2}\frac{\partial}{\partial r}\left(r^2\frac{\partial C}{\partial r}\right) \quad \textbf{Equation 2.9}$$

To solve this equation two boundary conditions were applied. First, at the edge of the spheroid r_0, the volume per unit mass of oxygen is equal to C_0. Second, at the distance denoted r_n (anoxic limit within the spheroid where oxygen cannot permeate), C is equal to 0. While, necrosis can have C values slightly above zero at r_n, it is close enough to zero, such that the model is not generally affected under this assumption [148]. Applying these boundary conditions Equation 2.10 is derived.

$$C(r) = C_o + \frac{a}{6D}\left(r^2 - r_o^2 + 2r_n^3\left(\frac{1}{r} - \frac{1}{r_o}\right)\right) \quad \textbf{Equation 2.10}$$

Finally, solving for r_n and setting $C(r_n)$ equal to zero, a fully analytical solution can be written in Equation 2.11. In the equation r_c is the viable region where both hypoxic and oxic cells are located [148].

$$2r_c^3 - 3r_o r_c^2 + \frac{6DC_o r_o}{a} = 0 \quad \textbf{Equation 2.11}$$

Th radius of an entirely viable spheroid is defined as r_l and is written in Equation 2.12. In this equation, p_o is the dissolved oxygen partial pressure at the surface of the spheroid, which is assumed to be equal to the bulk dissolved oxygen partial pressure. ρ_T is the density of the

spheroid, which is assumed to be the same as water, and ρ_{O2} is the density of oxygen gas, 1.331 kg m^{-3}. K is the Henry's Law constant previously calculated for oxygen concentration measurements of 1.04 mmol/L/atm.

$$r_l = \sqrt{\frac{6Dp_o}{a\rho_T \rho_{O_2} K}} \quad \textbf{Equation 2.12}$$

Equation 2.11 was solved using trigonometric identities to obtain Equation 2.13. The equation χ is written in terms of r_0, the radius of collagen spheroid.

$$\chi = \frac{arccos(1 - 2r_l^2/r_o^2) - 2\pi}{3} \quad \textbf{Equation 2.13}$$

The thickness of the anoxic region and the viable region are given in Equation 2.14 and 2.15, respectively [148].

$$r_c = r_o\left(\frac{1}{2} + \cos(\chi)\right) \quad \textbf{Equation 2.14}$$

$$r_n = r_o\left(\frac{1}{2} - \cos(\chi)\right). \quad \textbf{Equation 2.15}$$

The calculated r_n from the model developed by Grimes et al. was used to estimate the volume of the anoxic core region for a spherically shaped hydrogel. Figure 2.7 outlines the different radii and regions of the spheroid used in the calculations. Furthermore, this value was used to determine the percentage of the collagen hydrogel that is anoxic. Although the model is not a perfect geometric fit for the collagen hydrogels used, the model can provide an estimate for the anoxic region. Measured oxygen values were from the day 4 oxygen readings because cell viability and growth were evaluated on day 4 which provides a better

representation of the scaffolds. Since oxygen sensors were only placed after chamber 1, 5, and 6, the estimate of the anoxic core region was only calculated for chamber 1 and chamber 6 based on the empirical oxygen reuptake values for those chambers. The geometric dimensions used in model were from the day 4 hydrogel images as the dimensions are the smallest due to collagen compaction and least restrictive in terms of diffusional limitations.

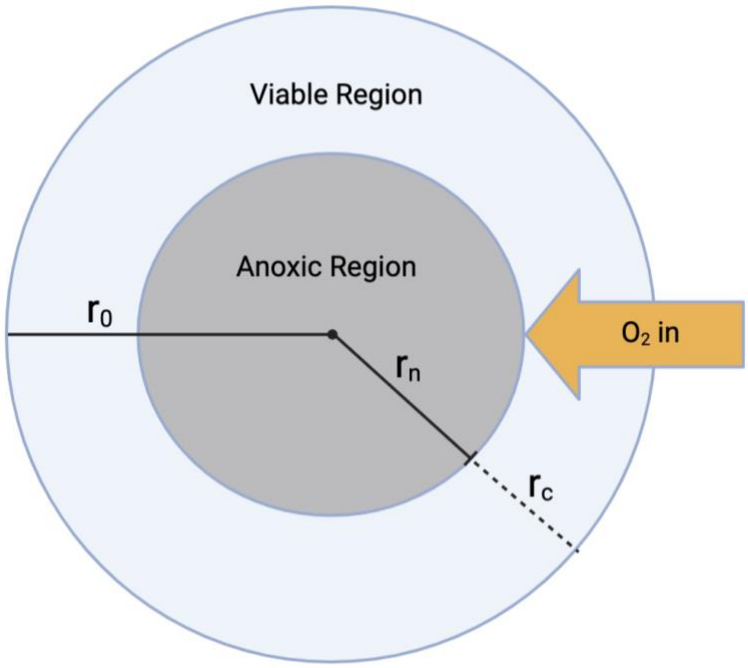


Figure 2.8: Anoxic Core Estimation Diagram

A diagram of the spheroid with radius r_0 for estimating the anoxic core region, with radius r_n and the viable region with shell thickness of r_c. The figure was adapted from the following publication and created in BioRender [148].

2.2.11 Cellular Quantification

During cell culture, collagen hydrogel formation and cell seeding, and at the 4-day mark of each bioreactor run, the number of cells was quantified. To do this, 100 µL of cell sample was stained with Trypan Blue (0.4% in solution; Sigma-Aldrich) and counted on a

hemocytometer. To count the cells, post bioreactor run, the hydrogels gels were transferred into a 24 well plate and digested using 0.5 mL per gel of 0.25% (w/v) collagenase type I in supplemented Waymouth Media for 2 hours. After full digestion, the cell suspensions were transferred into individual 15 mL Falcon tubes. Each well was washed with an additional 2 mL of fresh media and the washing media was transferred to the corresponding 15 mL tube. 100 μL of cell solution was retained for counting on a hemocytometer, as previously described. After quantifying the cells from each chamber, the cells were centrifuged for 5 minutes at 800 RCF. The supernatant was discarded, and cells were resuspended in Trizol reagent (Life Technologies). The cells were then stored in the -80°C freezer for later use.

2.2.12 Gene Expression

Gene expression was measured using quantitative real time polymerase chain reaction (qRT-PCR). Following the 4-day bioreactor run, the collagen hydrogels were digested, and the cells were quantified as outlined in section 2.2.11. The cells from chamber 1 and 6 in the series configuration and the cells of each chamber in the parallel configuration were homogenized using Trizol reagent (Life Technologies) per manufacturer's instruction. Next, the RNA was isolated using Direct-zol RNA MiniPrep kit (Zymo Research) per manufacturer's instructions. RNA concentration was quantified using nanodrop technology (BioTek Cytation5). The RNA was converted into cDNA via reverse transcription using qScript Ultra SuperMix (Quantabio) and Mastercycler nexus GX2 (Eppendorf). The cDNA was amplified using PerfeCTa SYBR Green FastMix (Quantabio) and specific genes using custom value DNA oligos (25 nmol, Life Technologies) listed in Table 1. All genes were normalized to a housekeeping gene glyceraldehyde 3-phosphate dehydrogenase (GAPDH). In the first analysis of gene expression, comparison between Chamber 1 and Chamber 6 was

conducted using the $2^{-\Delta\Delta Cq}$ method comparing target genes to GAPDH (ΔC_q) before comparing that change to a control experiment (Chamber 1) ($\Delta\Delta C_q$). A second analysis compared Chamber 1 and 6 to the parallel configuration using the $2^{-\Delta\Delta Cq}$ method comparing target genes to GAPDH (ΔC_q) before comparing that change to a control experiment (parallel configuration) ($\Delta\Delta C_q$).

Table 2.1: Gene Primer Sequences

List of gene primer sequences with their respective guanine to cytosine percentage (GC%). The length of targeting sequence (including primer length) was identified using SnapGene software.

	Forward Primer (5' to 3')	Reverse Primer (5' to 3')	GC% FP	GC% RP	Length
GAPDH	CATCACTGCCACCCAGAAGACTG	ATGCCAGTGAGCTTCCCGTTCAG	57%	57%	154 bps
HIF 1α	CCTGCACTGAATCAAGAGGTTGC	CCATCAGAAGGACTTGCTGGCT	52%	55%	102 bps
HIF 2α	GGACAGCAAGACTTTCCTGAGC	GGTAGAACTCATAGGCAGAGCG	55%	55%	128 bps
MMP3	CTCTGGAACCTGAGACATCACC	AGGAGTCCTGAGAGATTTGCGC	55%	55%	124 bps
MMP1a	AGGAAGGCGATATTGTGCTCTCC	TGGCTGGAAAGTGTGAGCAAGC	52%	55%	99 bps
PD1	CGGTTTCAAGGCATGGTCATTGG	TCAGAGTGTCGTCCTTGCTTCC	52%	55%	142 bps

2.2.13 Statistical Analysis

For all analysis at least three trials of series and 3 parallel chambers were utilized ($n \geq 3$). All results are reported as mean ± standard deviation. Statistical significance for the oxygen saturation and oxygen uptake rates per scaffold and per chamber were determined by a repeated measures two-way ANOVA with a Tukey HSD post hoc test to determine

significance between groups. Statistical significance of growth, viability, volume change, depth to anoxic core, and estimated anoxic core region was conducted using a Kruskal Wallis with Dunns post hoc test. Statistical testing for gene expression was conducted using a one-way ANOVA with Tukey HSD post hoc test or a student's t test, as appropriate.

2.3 Results

2.3.1 Measured Oxygen Saturation and Oxygen Uptake

As seen in Figure 2.6 representing the series configuration, the bulk media is not re-oxygenated as it flows through the downstream chambers before returning to the media reservoir. 2.9a presents the measured oxygen saturation levels after the exit of chamber 1, 5, and 6, throughout the 4-day bioreactor run. Chamber 2, 3, and 4 lacked a sensor and could not be monitored. The oxygen saturation level entering chamber 1 was confirmed to be 100% from previous measurements [147]. Figure 2.9b presents the measured oxygen levels at the exit of chamber 1 as well as the exit of the parallel chambers as shown in Figure 2.7. The parallel configuration is the standard bioreactor set-up for flow-perfusion bioreactors. Additionally, the oxygen level entering each chamber of the parallel configuration is 100% since the tubing throughout the flow-perfusion system is oxygen permeable and the glass media reservoirs allow for the complete reoxygenation of the circulating media. A comparison between the oxygen levels exiting the parallel chambers and chamber 1 of the series set-up, shown in Figure 2.9b, show no significant differences for the duration of the experiment. The oxygen saturation after 4 days of culture for chamber 1 dropped ~26%. The average oxygen saturation drop after chamber 6 (the chamber expected to receive the greatest sub-saturation oxygen level) was ~36%. The average oxygen saturation drop between

chambers 5 and 6 was ~3%. Between day 1 and day 4, the oxygen saturation levels dropped for each chamber location, but these differences were not statistically significant for any location.

From these oxygen saturation measurements, the average oxygen consumption per scaffold and per cell was noted for chamber 1 and chamber 6, as displayed in Figure 2.10a and Figure 2.11a. Uptake measurements were only reported in chamber 1 and chamber 6 because the oxygen saturation of the entering and exiting media were only known in these two chambers. They do serve as potential extremes of chambers that receive fully oxygen saturated media (chamber 1) and media with the lowest level of oxygen saturation (chamber 6). The oxygen consumption of chamber 6 did not significantly change over the 4 days. However, the oxygen consumption of chamber 1 increased 290% per cell and 255% per scaffold. The average oxygen consumption per scaffold and per cell was noted for chamber 1 in contrast to the parallel configuration in Figure 2.10b and Figure 2.11b. The parallel configuration maintains a similar increase in average oxygen consumption per cell and per scaffold as chamber 1 furthering the confirmation that chamber 1 experiences similar culturing conditions to the scaffolds cultured in the standard parallel format for traditional tissue engineering experiments.

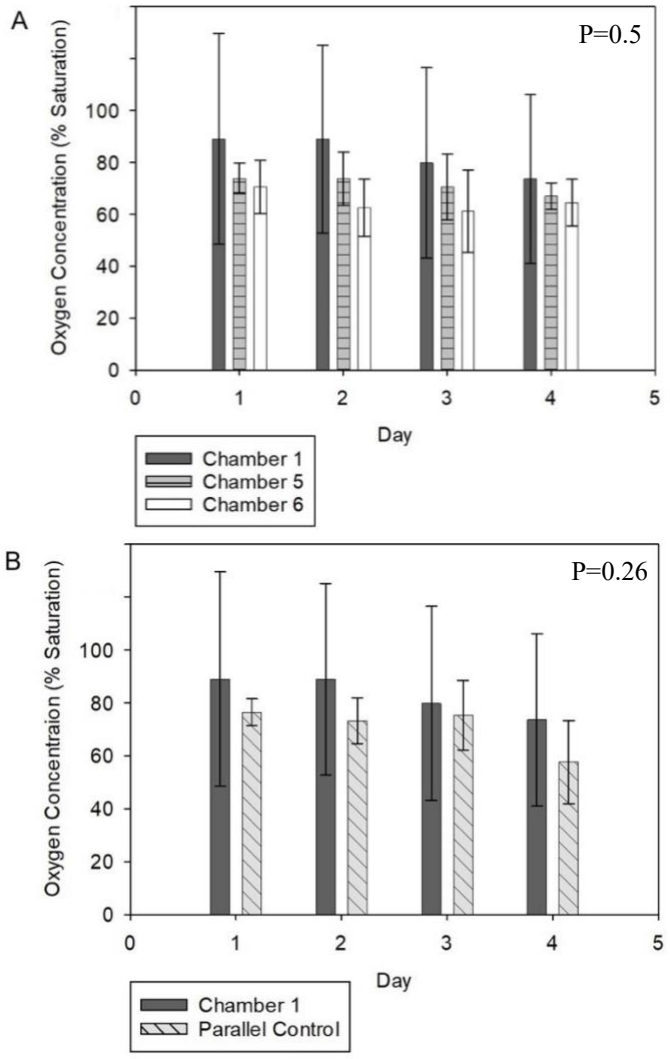


Figure 2.9: Oxygen Saturation of Series and Parallel Configuration

(A) Percent oxygen saturation was measured from the bulk media after chamber 1, chamber 5, and chamber 6 for 4 days. In the series configuration, the bulk media dissolved oxygen concentration surrounding the hydrogel scaffolds varies as the media flows to downstream chambers. (B) Percent oxygen saturation measurement of bulk media after chamber 1 compared to the bulk media saturation of the parallel configuration for 4 days. Two-way ANOVA was conducted with an α*=0.05 and Tukey Honesty Significant Difference (HSD) post hoc test. Data is represented as mean* $\pm$ *standard deviation (SD),* $n \geq 3$*. Over the 4 days, there is a decrease is oxygen saturation for chambers 1, 5, and 6, however this decrease is not statistically significant (P=0.5). The parallel configuration compared to chamber 1 followed the same decrease in oxygen saturation with not statistical significance (P=0.26).*

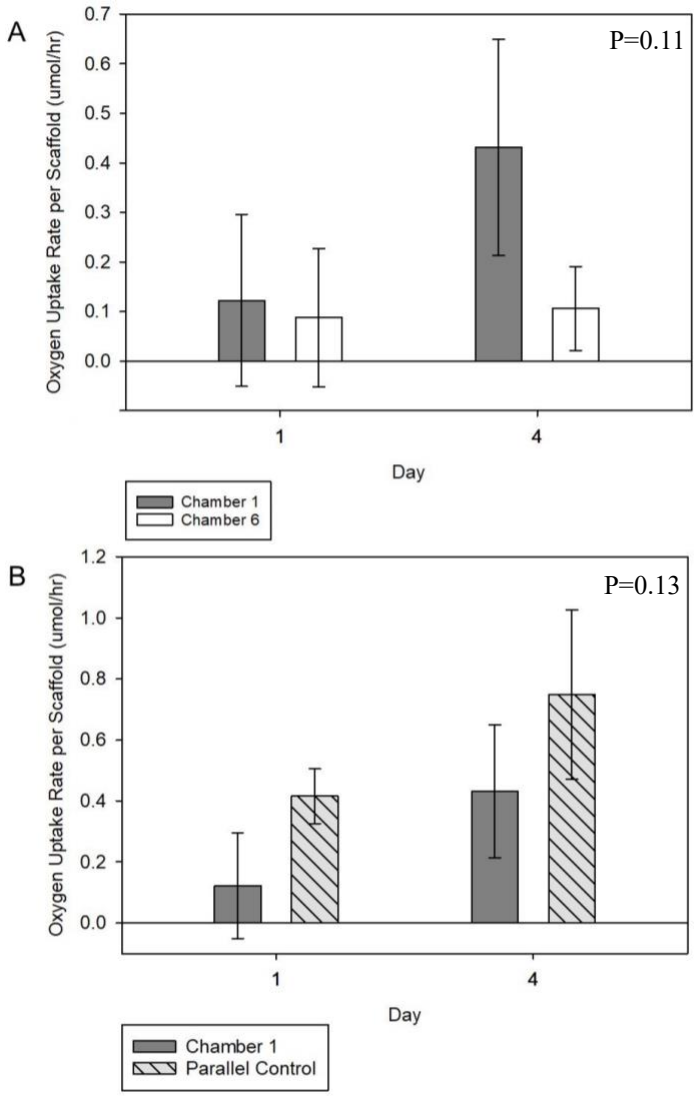


Figure 2.10: Oxygen Consumption per Scaffold

(A) Each bar represents the average uptake rate of oxygen per scaffold on day 1 and day 4 for chamber 1 and chamber 6. (B) Comparison of oxygen uptake rates for chamber 1 and the parallel configuration. Values are reported in μmol/hr. Calculations were made based on the concentration of oxygen as specified by Bryant et al. and Felder et al [144], [147]. Two-way ANOVA with an α=0.05 was conducted with a Tukey Honesty Significant Difference (HSD) post hoc test. Data is represented as mean ± SD, n≥ 3. By day 4, the average oxygen consumption rate for chamber 1 is larger than chamber 6 (p=0.11) but still not statistically significant. On day 4 there is no significant difference between chamber 1 and the parallel control (p=0.13).

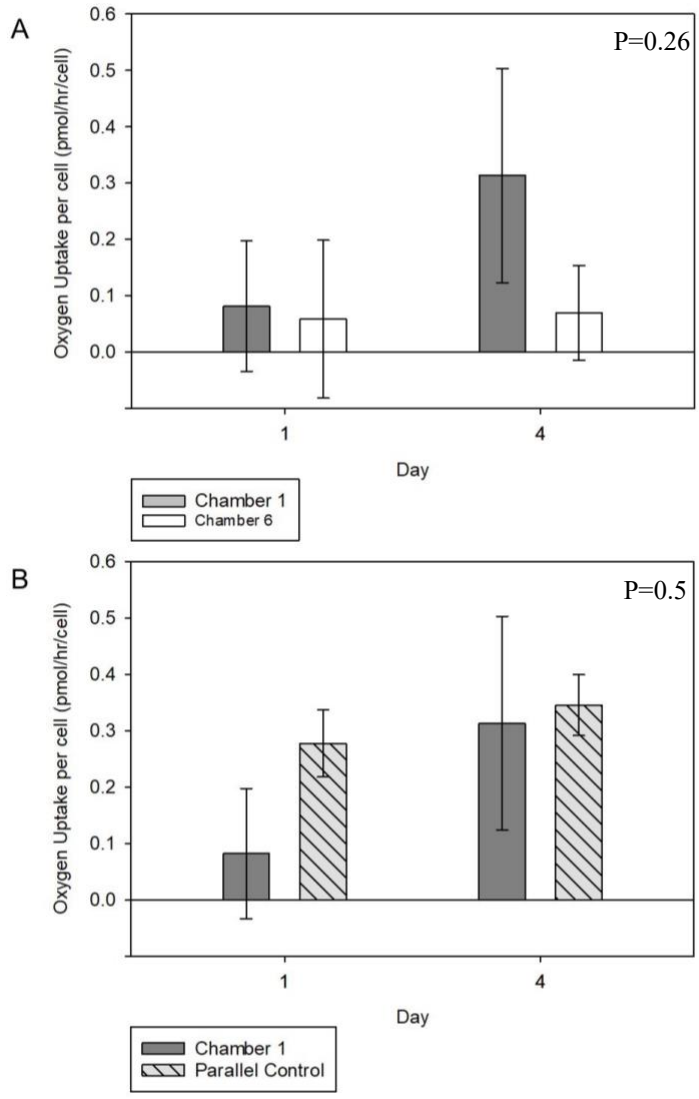


Figure 2.11: Oxygen Uptake Rate per Cell

(A) Each bar represents the average uptake rate of oxygen per cell on day 1 and day 4 for chamber 1 and chamber 6. (B) Comparison of the oxygen uptake rate per cell of chamber 1 and the parallel configuration. Values are reported in pmol/hr/cell. Calculations were made based on the concentration of oxygen as specified by Bryant et al. and Felder et al [144], [147]. Two-way ANOVA with an α=0.05 and a Tukey Honesty Significant Difference (HSD) post hoc test. Data is represented as mean $\pm$ SD, n$\geq$ 3. By day 4, the average oxygen consumption rate for chamber 1 is larger than chamber 6 (p=0.26) but still not statistically significant. On day 4 there is no significant difference between chamber 1 and the parallel control (p=0.5).

2.3.2 Cell Growth and Viability

The final percent cell growth and viability were quantified for each chamber hydrogel after 4 days to determine the effect of variable oxygen saturation on the proliferation rate. Figure 2.12a presents the average percent growth and Figure 2.13a presents the average viability for the series (sub-saturation oxygen) Chamber 1, 5, and 6. As the chamber number increases, there is generally a decrease in growth and viability compared to chamber 1, but that decrease is not statistically significant. Chamber 6 experienced and average of ~13% growth compared to the ~45% growth in chamber 1. Further, the viability of chamber 6 decreases ~20% compared to chamber 1 as the oxygen saturation decreases. Figure 2.12b presents the average percent growth and Figure 2.13b presents the average viability for Chamber 1 and parallel configuration. The average percent growth and viability for chamber 1 and the parallel configuration are comparable with ~43% to 45% growth and 74% to 82% viability. Thus, confirming the growth and proliferation activities within chamber 1 and the parallel configuration are similar.

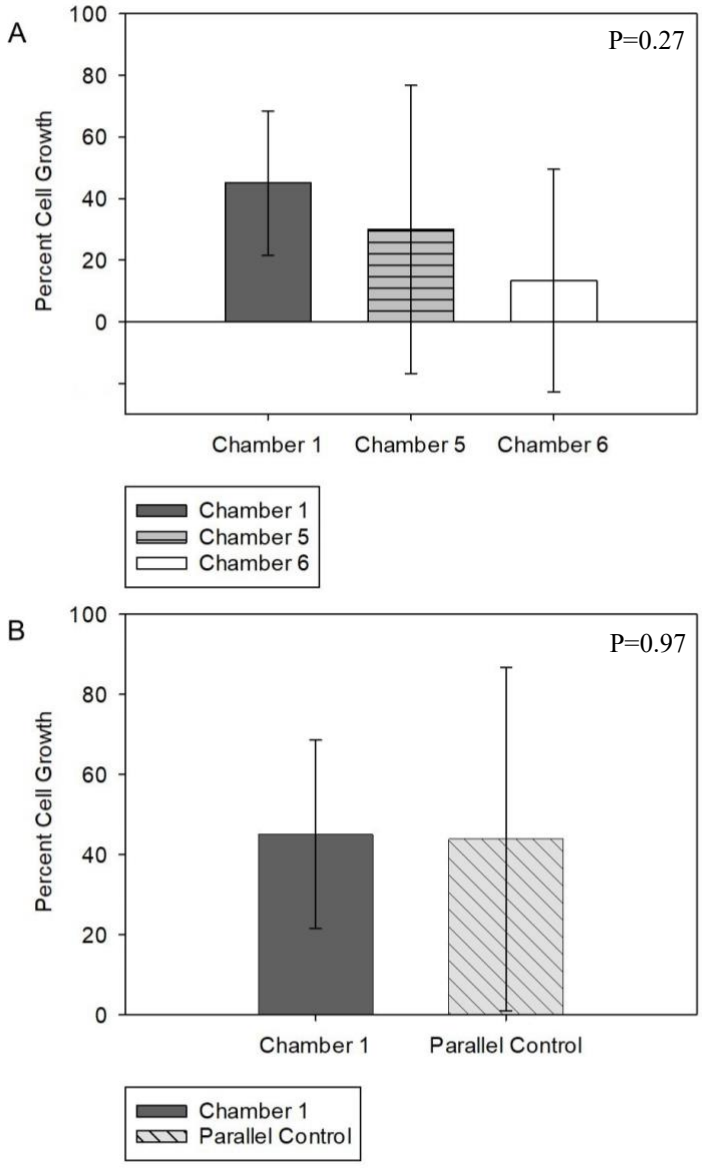


Figure 2.12: Percent Growth of Cell Scaffolds

(A) Cells were quantified for chambers 1, 5 and 6 and used to calculate percent growth over the 4-day culture. (B) Percent growth of chamber 1 and the parallel configuration. In the series configuration, the oxygen saturation decreased as the chamber number increased. However, the average cell growth was variable from run to run. A Kruskal-Wallis Statistical test with a significance value of 0.05 was conducted with Tukey HSD post hoc test. Data is represented as mean ± SD, n≥ 3. By day 4, the cells in chamber 1 experience greater growth than cells in chamber 6 (p=.27), but not statistically significant. The viability between chamber 1 and the parallel control was not statistically significant (p=0.97).

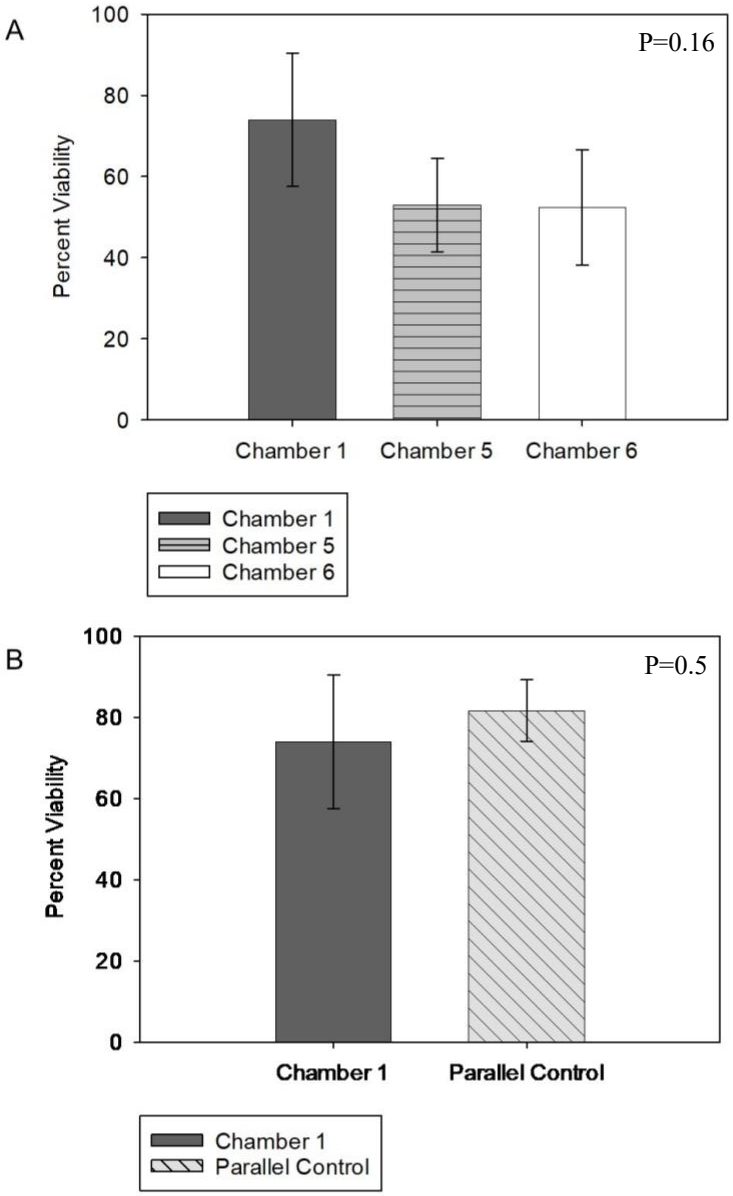


Figure 2.13: Percent Viability of Scaffolds

The Cell viability was calculated as (Live Cells/(Live Cells + Dead Cells))100%. (A) Percent cell viability for chambers 1, 5, and 6. (B) Percent viability for Chamber 1 and the parallel configuration. A Kruskal-Wallis Statistical test with a significance value of 0.05 was conducted with Tukey HSD post hoc test. Data is represented as mean ± SD, n≥ 3. By day 4, the cells in chamber 1 experience greater viability than cells in chamber 6 (p=0.16), but not statistically significant. The viability between chamber 1 and the parallel control was not statistically significant (p=0.50).

2.3.3 Hydrogel Dimensions and Anoxic Core Estimation

Each hydrogel's dimensions changed throughout the 4-day bioreactor run for both the series and parallel configuration. These changes are most likely owed to the cellular remodeling and collagen contraction and the perfusion flow of media through the gels. The volumetric change was measured using ImageJ software and a scale bar. The dimensional measurements are noted in Table 2.2. The average percent change for each chamber in the series configuration are displayed in Figure 2.14a based on the original 0.5 mL volume on day 0. The percent changer per chamber was feasible due to ability to measure each scaffold's dimensions. The greatest average percentage volumetric change was 76% (chamber 4 and 6), with the smallest average percent change 69% (chamber 2). Figure 2.14b shows the average percent volume change for chamber 1 of the series configuration compared to the parallel configuration. The percent volume change between the parallel configuration and chamber 1 are close in value with a difference of ~5% volume change. For all the hydrogels used in the four-day culture period, the volume change varied between 66% and 76%, but no statistical differences were identified between all scaffold chambers, including the parallel set-up. The overall average shrinkage after 4 days of culture for all chambers was 72%.

Table 2.2: Hydrogel Dimensions and Volume

Hydrogel dimensions were measured in mm for the length, width, and height of each scaffold chamber for the series and parallel configurations. The volume was calculated using the formula for an elliptical cylinder.

	Chamber	L(mm)	w(mm)	h(mm)	V (mm^3)	V(cm^3 or mL)
Series Trial 1	**1**	5.486	5.259	3.087	279.799	0.280
	2	4.87	5.901	2.725	246.020	0.246
	3	3.845	4.977	2.432	146.210	0.146
	4	2.563	4.726	1.812	68.953	0.069
	5	6.05	3.913	2.432	180.875	0.181
	6	6.093	4.004	1.848	141.637	0.142
Series Trial 2	**1**	3.948	4.392	1.779	96.909	0.097
	2	3.536	5.7	1.944	123.093	0.123
	3	3.622	4.722	2.39	128.417	0.128
	4	3.654	5	2.86	164.155	0.164
	5	5.556	4.176	1.964	143.157	0.143
	6	3.928	3.654	2.24	101.004	0.101
Series Trial 3	**1**	3.889	2.704	1.458	48.167	0.048
	2	5.46	4.609	1.118	88.388	0.088
	3	3.259	5.099	2.136	111.512	0.112
	4	3.75	4.756	2.15	120.465	0.120
	5	4.007	4.007	2.305	116.268	0.116
	6	4.507	3.758	2.15	114.402	0.114
Parallel Trial 1	**1**	4.235	5.919	2.779	218.847	0.219
Parallel Trial 2	**1**	6.483	4.816	1.625	159.392	0.159
Parallel Trial 3	**1**	5.44	3.384	2.246	129.894	0.130

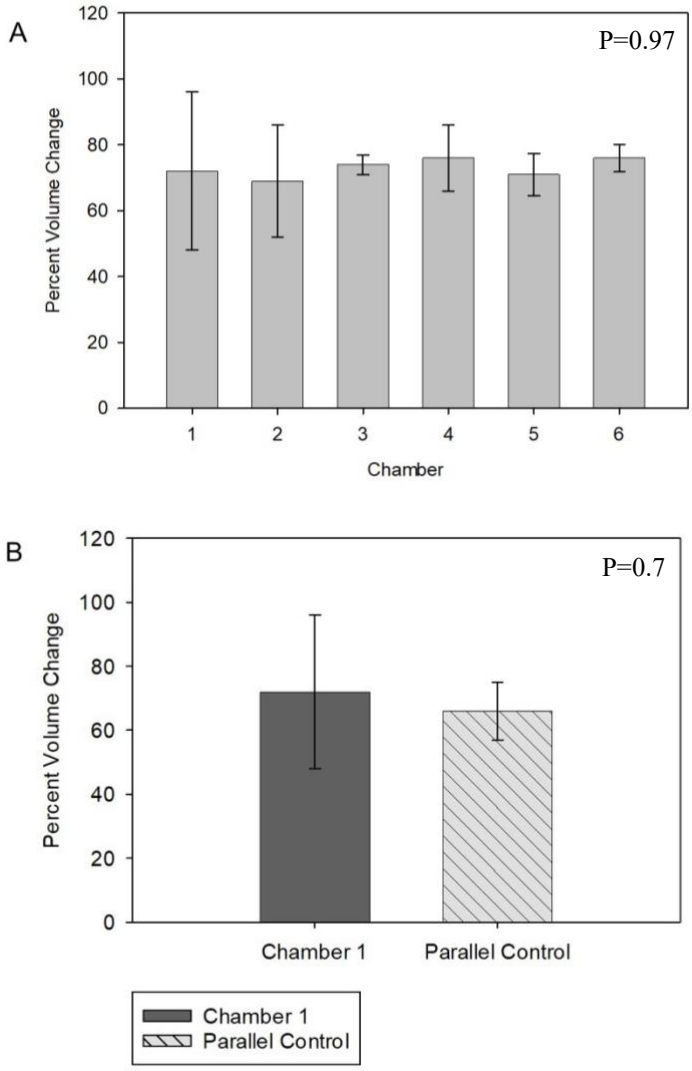


Figure 2.14: Percent Volume Change of Hydrogel Scaffolds

(A) The percent of volumetric change per scaffold in the series for all chambers calculated using the initial seeding volume of 0.5 mL. Note all chambers are represented by the color gray. The numbers on the axis correspond to the Chamber number of the series configuration. (B) Percent volume change for chamber 1 and the parallel configuration, calculated the same as part A. A Kruskal-Wallis Statistical test with a significance value of 0.05 was conducted with Tukey HSD post hoc test. Data is represented as mean ± SD, n≥ 3. There was no significant significance across all 6 chambers in the series configuration (p=0.97). There is no statistical significance between chamber 1 and the parallel control under a student t-test (p= 0.7).

An estimation of the hypoxic core region was done using a modified spheroid model. Figure 2.15a contains the estimated average depth to reach the hypoxic core region, r_c, for chamber 1 and 6 in the series configuration. Chamber 6 is estimated to have a much shorter average depth to the anoxic core region ~100 μm. The decrease in depth to the anoxic core region corresponds to the decrease in cell viability and growth. Figure 2.15b contains the estimated average depth to reach the hypoxic core region, r_c, for chamber 1 and the parallel configuration. The estimation for the parallel and chamber 1 average depth are similar in value furthering the sentiment that the culture conditions are similar. Figure 2.16a outlines the average predicted percentage of the anoxic spheroid volume from the calculated r_n values for chambers 1 and 6. The percent hypoxic volume of chamber 6 is ~22% larger than the percent hypoxic volume of chamber 1, indicating as the oxygen saturation drops, the percent hypoxic volume increases. Figure 2.16b outlines the predicted percentage of the anoxic spheroid volume from the calculated r_n values for chamber 1 and the parallel configuration. Interestingly, the parallel configuration is estimated to have a smaller average hypoxic core region compared to chamber 1 of the series configuration.

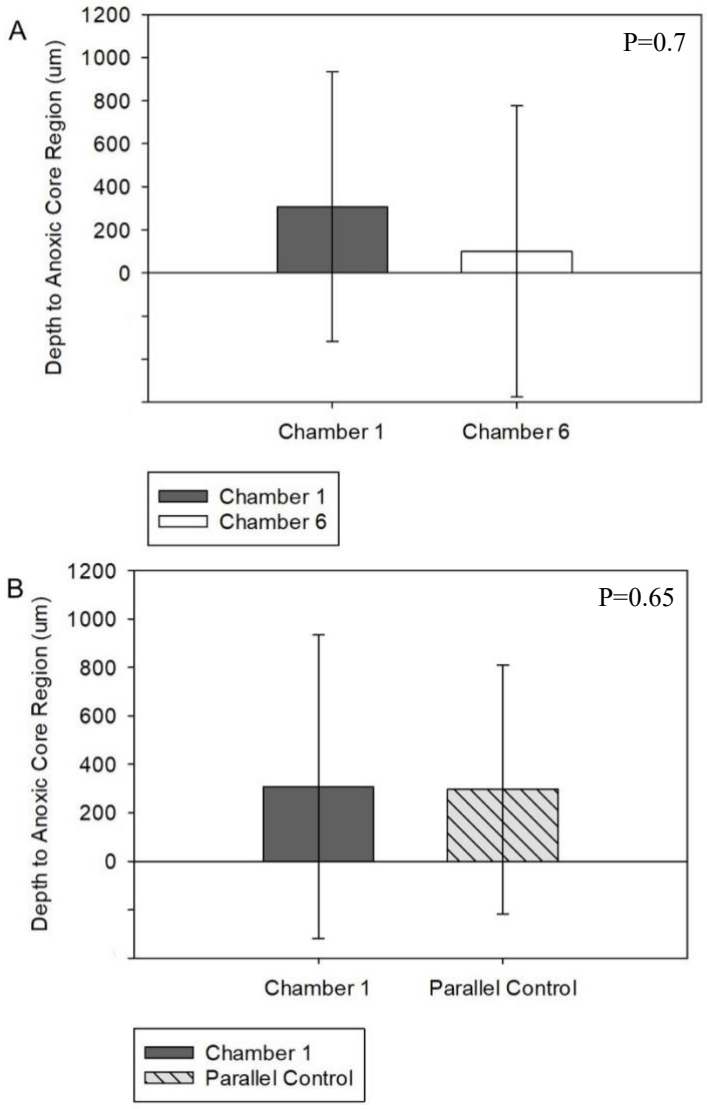


Figure 2.15: Estimated Depth to Anoxic Core Region of Hydrogel Scaffold

(A) Using the hypoxia model, the depth to the hypoxic region of each scaffold was calculated for chamber 1 and 6. As the chamber number increases, the oxygen saturation decreases alongside a decreased in depth to the anoxic core region. (B) Estimated depth to the hypoxic core of chamber 1 and the parallel configuration. A Kruskal-Wallis Statistical test with a significance value of 0.05 was conducted with a Tukey HSD post hoc test. Data is represented as mean ± SD, n≥ 3. There is a shorter depth to reach the anoxic core region in chamber 6 compared to chamber 1, but lacked statistical significance (p=0.7). There is no statistical significance between the parallel configuration and chamber 1 depth to reach the surface of the anoxic core region (p=0.65).

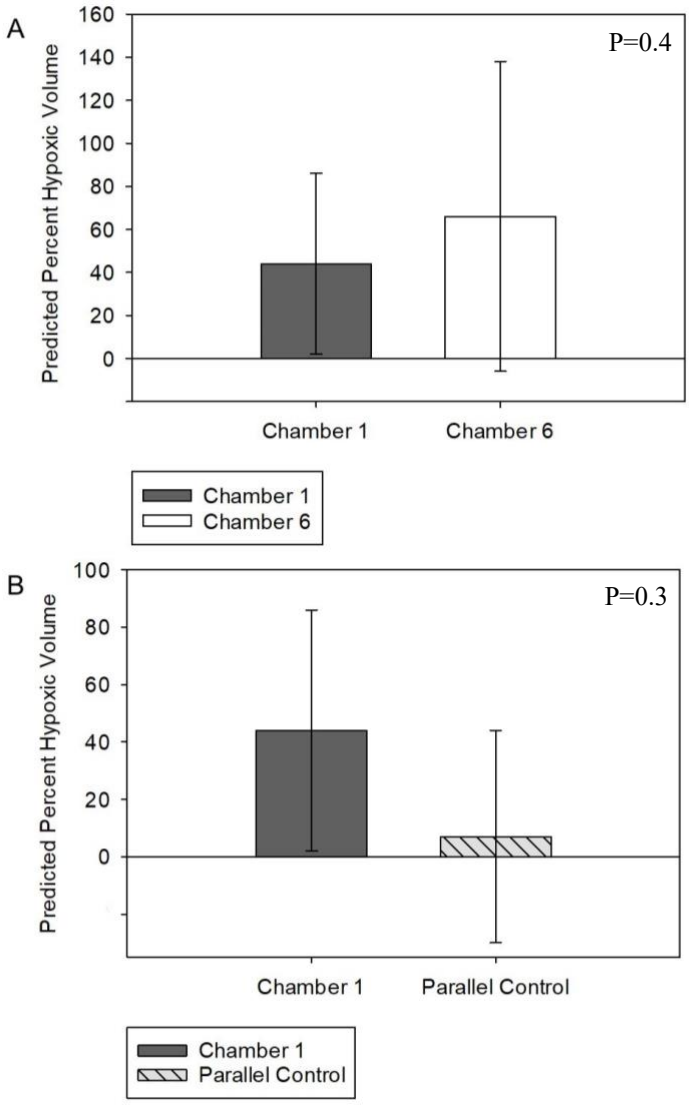


Figure 2.16: Model Predicted Percentage of Anoxic Volume

(A) Estimated depth to the anoxic core region of Chamber 1 and Chamber 6. (B) Estimated depth to anoxic core region of Chamber 1 and the parallel configuration. The percentage of the total hydrogel volume calculated to be anoxic based on the predicted r_n value and the spherical volume formula. The total volume was calculated using the hydrogel heights as the diameter of the sphere. A Kruskal-Wallis Statistical test with a significance value of 0.05 was conducted with Tukey HSD post hoc test. Data is represented as mean ± SD, n≥ 3. The model predicts higher anoxia in chamber 6, but is not statistically significant (p=0.4). The estimated percent volume of the anoxic core region is smaller for the parallel configuration than chamber 1, but not statistically significant (p=0.3).

2.3.4 Gene Expression

Figure 2.17a shows the gene expression of chamber 6 relative to chamber 1 after 4 days of culture. The $2^{-\Delta\Delta Ct}$ method was used with $\log_2$ transformation. HIF-1α and PD1 were upregulated. However, PD1 has a greater upregulation than HIF-1α. Additionally, MMP3, MMP1a, and HIF-2α were down regulated relative to chamber 1. Figure 2.17b shows the gene expression of chamber 1and chamber 6 relative to the parallel control at the end of the 4-day bioreactor run. The $2^{-\Delta\Delta Ct}$ method was used with $\log_2$ transformation. HIF-1α was increased in both chamber 1 and chamber 6 at a similar fold change. However, both chambers 1 and 6 were significantly increased compared to the parallel configuration control. Interestingly, HIF-2α , known for expression in extended periods of low oxygen concentration, was significantly downregulated in both chambers 1 and 6 at similar expression levels compared to the parallel control. Looking at the genetic expression of known genes for disease progression and metastasis, MMP3 and MMP1a were upregulated in both chamber 1 and 6 compared to the control. However, in chamber 1, MMP3 was significantly upregulated compared to its expression in chamber 6. Additionally, MMP1a was upregulated significantly in chamber 6 compared to chamber 1 and the control. PD1 was upregulated compared to the control for both chambers, but chamber 1 was upregulated significantly higher than chamber 6

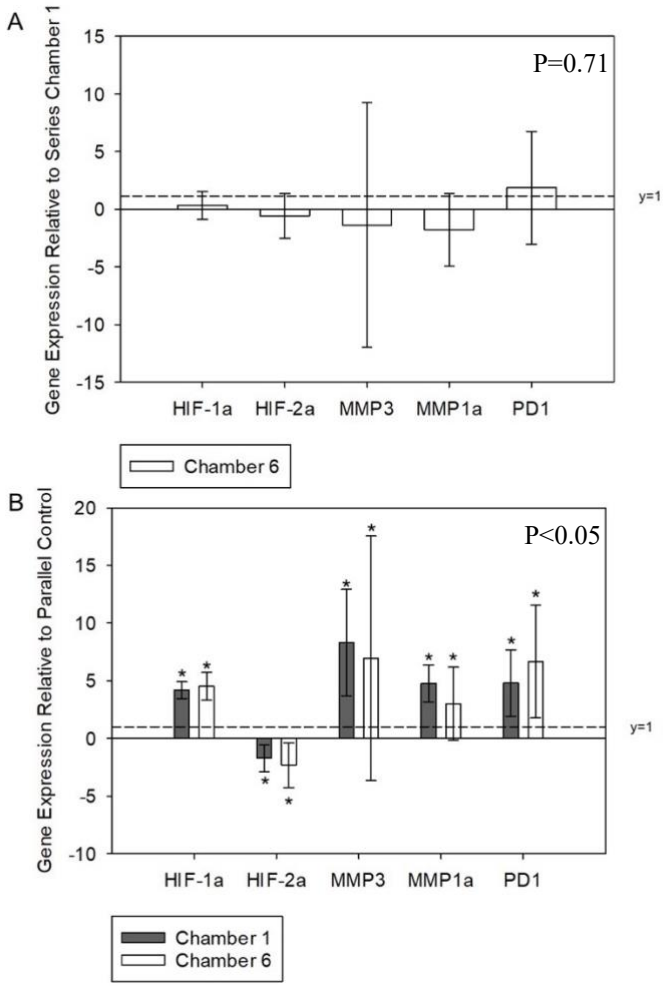


Figure 2.17: Genetic Expression of Hypoxia and Disease Progression Genes
*(A) QRT-PCR results for chamber 6 after 4 days of recirculated media compared to the Chamber 1 control. The data displayed is $\log_2$(Fold Change) using the $2^{-\Delta\Delta Ct}$ methodology. The Chamber 1 control is noted as a dashed line at a genetic expression level of 1. A student's t- Test was used to test for significance. Data is represented as mean ± SD, n≥ 3. (B) QRT-PCR results for both chamber 1 and chamber 6 after 4 days of recirculated media compared to the parallel configuration control. The data displayed the same as described in (A). The parallel control is noted as a solid line at a genetic expression level of 1. A one-way ANOVA with an α=0.05 and a Tukey post hoc test was conducted and significance from the parallel is denoted by *. Data is represented as mean ± SD, n≥ 3. It is important to note that in (B), statistical significance (*) is relative to the parallel configuration and not between chambers 1 and 6 ($p<0.05$). There is no statistical significance between chamber 1 and 6 ($p=0.14$).*

2.4 Discussion

Every day during the 4-day bioreactor experiment, the oxygen saturation of the bulk media was measured, averaged, and plotted versus time in Figure 2.9a, which shows a general decrease in oxygen saturation over time. It is important to note, there is a decrease in oxygen saturation over day 1 and 2, then the oxygen saturation increases on day 3 before decreasing again on day 4. These changes ranged between -18% and 4% and were not statistically significant. These observations are likely the result of the high initial cell seeding value of 1.5 million cells per scaffold. The typical seeding density for collagen type I hydrogels given the final volume ranges from 300,000 to 1.5 million cells which demonstrates that the seeding density used in this experiment operated very near the upper limits of cell seeding capacity for collagen type I hydrogels with a density of 4 mg/ml [150]. Significantly lower cell seeding densities were not practical due to the sensitivity of the oxygen sensor. The limited ability of cell growth within these hydrogels resulted in reaching cell saturation by day 2 and 3 and even observe cell death in some cases which decreases the amount of oxygen consumed. Additionally, the oxygen drop within individual chambers on a daily basis was smaller in chambers 5 and 6 compared to the daily drop in chamber 1, which is most likely due to the increased hypoxic region of the scaffolds in downstream chambers and the decrease in oxygen saturation. This means the availability of oxygen into the scaffolds became limited where the innermost seeded cells could not consume oxygen or could not consume oxygen as efficiently as cells located on the periphery of the scaffold. Thus, a smaller delta oxygen for chambers 5 and 6 was noted due to the proportion of oxygen consuming cells. This is explained further in Figure 2.10a and 2.11a where the average per scaffold and per cell oxygen uptake rates for chamber 1 and chamber 6 are noted. On day 1,

the average oxygen consumption in chamber 1 shows slightly higher per scaffold and per cell oxygen consumption compared to chamber 6, without any statistical significance. By day 4, the average oxygen consumption rate for chamber 1 is larger than chamber 6 ($p=0.11$) but still not statistically significant. Over the 4 days, the average oxygen consumption per scaffold and per cell of chamber 6 increases slightly but largely remains constant. One key difference between the two chambers is the viability and growth calculated on day 4, which is noted in Figures 2.12a and 2.13a. The calculation for oxygen uptake rate follows the assumption that all cells within a hydrogel consume oxygen at the same rate. The cells in chamber 1 experience greater growth than cells in chamber 6 ($p=.27$). This could indicate an altered metabolism for oxygen consumption due to the lower bulk oxygen saturation. Further, since no measurement of cell death is recorded for days 1 to 3, the oxygen uptake rate on a per cell basis maybe slightly underestimated. The parallel control followed the same general trend of decreasing oxygen saturation over the 4-day bioreactor run with minimal decrease in oxygen saturation drop between day 2 and 3 as shown in Figure 2.9b. Figure 2.12b and 2.13b suggest the viability and growth of the cells in the parallel configuration are similar to chamber 1. Interestingly, the oxygen uptake per scaffold and per cell for the parallel configuration is greater than chamber 1 for day 1 ($p=0.06$) but almost identical on day 4. Although chamber 1 experiences the same oxygen saturation conditions as the parallel configuration, a difference between the two set ups that needs to be noted is the exposure of cells to circulating signaling molecules secreted by downstream chambers in the series setup.

The effect of sub-saturation oxygen levels on cell proliferation and viability were also assessed. Figure 2.12a presents the cellular growth in chambers 1, 5, and 6 after 4 days as an average percent growth. This shows a negative trend in cell growth as the oxygen saturation

level decreases. This observation agrees with the presence of a larger hypoxic/necrotic core in downstream chambers. The results appear noisy preventing any statistical comparison leading to valuable conclusions. The observed noise maybe due to the inconsistent shrinkage of the individual hydrogels evident from the variations observed in the final hydrogel volumes presented in table 2.2 where the shrinkage levels varied significantly in hydrogels that were expected to have small variabilities in cellularity. Additional differences in scaffold shape contributed to variations in cell growth as the hydrogel shape affects oxygen concentration gradients and as a result survival. Figure 2.12b shows chamber 1 growth is similar to the parallel control growth, indicating the proliferation and growth conditions of chamber 1 were like those of the parallel configuration control. Further, the average viability was calculated in Figure 2.13a for chambers 1, 5, and 6. The average viability decreases as the oxygen saturation decreases. Chamber 5 and 6 maintain similar average viability percentages. The change in viability between the two consecutive chambers (5 and 6) does not appear to be significant enough to overcome the expected noise from hydrogel shape, volume, and seeding characteristics. The dimensions and volume change of each chamber is outlined in Table 2.2 and Figure 2.14a and 2.14b. The viability change between chamber 1 and 6 is large but experiences significant noise ($p=0.16$). It is a potential indication of an increasing hypoxic core for scaffolds downstream the series set up. When comparing chamber 1 to the parallel control, the viability is similar according to Figure 2.13b. This further suggests the validity of the growth conditions between chamber 1 and the parallel control, with the obvious variation of the presence of secreted biomolecules from all chambers in the series set up.

To evaluate the accuracy and repeatability of the *in vitro* model, the shape and size of the anoxic core region is required. Table 2.2 contains the dimensions of each scaffold from 3 series and 3 parallel configuration scaffolds. After the 4-day bioreactor run, the scaffolds most closely resembled an elliptical cylinder due to the PLLA mesh scaffold holder that was shaped as an elliptical cylinder. The volumes of the hydrogels drastically changed compared to the initial 0.5 mL hydrogel volume. The average percent change for all 6 scaffolds in series and parallel configuration are shown in Figure 2.14a. The hydrogel scaffold shrinkage is expected due to the cell-ECM forces with the additional effect of fluid flow on hydrogel deformation that is not expected to be the dominant factor but it may still influence hydrogel shrinkage [151], [152]. The variability seen in Figure 2.14a is not denoting any effect from the position of each hydrogel in the 6 chambers in series. Since the cellularity differences between chambers are not substantial, shape and size variations of hydrogels can vary due to inconsistences in the formation of gels during different experimental runs and even effects of hydrogel swelling despite the use of a hydrogel mold. These differences in gel formation and characteristics can affect the nutrient diffusion within the scaffold. As mentioned previously, these differences can affect the growth and viability of seeded cells. The differences in gel formation were controlled by creating a "master mix" of collagen, neutralizing solution, and cell solution. The parallel control showed the greater average percent volume change despite having similar viability and growth to chamber 1, as noted in Figure 2.14b. After having calculated the shape of each hydrogel at the endpoint of culture (day 4) the estimation of the hypoxic/necrotic core extent is conducted.

To estimate the hypoxic/necrotic core region, a spheroid model was adapted as described in section 2.2.10 by applying empirically measured data from the oxygen uptake rates of

EMT6 cells and the diffusion of oxygen in high density collagen hydrogels (4mg/mL). Although the shape of the hydrogels does not exactly match the spheroid geometry of the estimation model, the model shows the oxygen saturation level drop to anoxic levels and provides an estimated depth to the starting point of the anoxic core within the scaffold. The comparison of the anoxic core region volumes is performed because they mirror the depth from the hydrogel surface where viability is compromised, with greater anoxic volumes associated with shorter depth distance to the region. The predicted depth where the anoxic core starts is shown in Figure 2.15a for chambers 1 and 6. The model predicts higher anoxia in chamber 6, which is confirmed by the cell viability and growth, but is not statistically significant ($p=0.4$). Figure 2.15b compares the predicted depth of the anoxic core in the hydrogel of chamber 1 and the parallel configuration. The average depth of the anoxic core region is similar for the parallel configuration and chamber 1, suggesting similar normoxic oxygen saturation levels. The average percent volume of the anoxic core region for chambers 1 and 6 are shown in Figure 2.16a. The larger average anoxic core region estimated for chamber 6 agrees with the shorter depth to reach this region and increased size compared to chamber 1, but lacked statistical significance ($p=0.7$). These estimations are consistent with larger expected hypoxic regions in low oxygen culture conditions. Figure 2.16b compares the percent volume of the anoxic core region between chamber 1 and the parallel configuration. The estimated percent volume of the anoxic core region is smaller for the parallel configuration than chamber 1, but not statistically significant ($p=0.3$). Difference in cell signaling within the series configuration may be behind this observation.

In order to evaluate the molecular effect of sub-saturation oxygen levels on EMT6 cell line, QRT-PCR was conducted, which is crucial in understanding the changes in metabolism

and disease progression as seen in 2D *in vitro* models. As previously noted, HIF-1 and HIF-2 are transcriptional regulators for genetic modifications under hypoxic conditions. As such, the gene expression was measured and shown in Figure 2.17a and 2.17b. HIF-1α is considered the "master regulator" for acute and short-term hypoxia. Thus, the upregulation in chamber 6 indicates there is successful sub-saturation of oxygen levels present and pathway activation. However, the stronger upregulation seen in chamber 1 suggests stronger HIF-1α stabilization, which could be due to cell signaling molecules released to the media from downstream chambers, as the media is recirculated and not replaced over the 4-day culture period. For example, the chamber with the theoretically greatest sub-saturation oxygen level could release signaling molecules related to stress that are then circulated into the bulk media for cellular signaling in chamber 1. This circulation of signaling molecules was not the primary focus of the study and requires further research to analyze the effect. Additionally, based on the estimation of the anoxic core region, there are cells present within this region experiencing oxygen starvation leading to an increased HIF-1α expression in chamber 1. Interestingly, HIF-2α was down regulated in both Chamber 1 and Chamber 6. HIF-1α is associated with rapid and acute hypoxia, while HIF-2α generally is associated with long term hypoxia. Unlike HIF-1α, HIF-2α is associated with involvement in stemness, erythropoiesis, and immune modulation. The down regulation of HIF-2α in Figure 2.17a and 2.17b could indicate the sub-saturation of oxygen in the bulk media is not chronic enough for HIF-2α stabilization.

Given the upregulation of HIF-1α, downstream HIF-1α regulated targets were also analyzed. Three common downstream targets MMP3, MMP1a, and PD1 were also upregulated in both chamber 1 and 6, with the parallel set up as control, which further

confirms cellular adaptations to sub-saturation oxygen levels and HIF-1α stabilization. MMP3 and MMP1a are collagenases known to aid cancer cells metastasis through matrix remodeling in response to hypoxia. The upregulation of MMP3 and MMP1a confirms activation of tumor response pathways to sub-saturation oxygen levels as cancer cells metastasize for easier access to oxygen supply [153], [154]. Further, the upregulation of PD1 indicates a greater potential for immune system evasion under stress conditions [155]. Concurrently, the upregulation of these downstream targets to HIF-1α indicate immunosuppressive and pro-metastatic pathways in response to sub-saturation oxygen. The greater increase in both MMP3 and MMP1a in chamber 1 could potentially suggest the cells are favoring an invasion and metastatic pathway upregulation. While the greater increase in PD1 of chamber 6 could suggest the cells are favoring immunosuppressive pathways. These sentiments were noted in Figure 2.17a, where MMP3 and MMP1a were downregulated relative to chamber 1.

2.5 Conclusion

The primary goal of this study was to incorporate different levels of sub-saturation oxygen conditions in a modified bioreactor. EMT6 cell line was used to create an *in vitro* solid tumor model to analyze the effect of sub-saturation oxygen levels. Bulk media oxygen saturation was measured using previously optimized fluorescent optical oxygen sensors and a previously modified flow-perfusion bioreactor. 3D collagen hydrogel scaffolds were used to create the solid tumor model. While the 3D tumor models are more representative of tumor pathophysiology, the effect of sub-saturation oxygen levels induced in a flow-perfusion bioreactor has not been incorporated in previous studies. Given the importance of the solid tumor microenvironment on disease progression and the hypoxic hallmark of solid TME

requires more accurate *in vitro* culture systems. Varying oxygen concentrations were generated inside the bioreactor using oxygen impermeable tubing to prevent reoxygenation of bulk media flowing through consecutive scaffold chambers connected in series. Thus, a stepwise drop of oxygen was created. Optical sensors were placed after chamber 1, chamber 5, and chamber 6 to strategically measure the oxygen concentrations at 100% saturation at the entrance of the chamber 1 and the parallel chambers and the most extreme sub-saturation of oxygen, chamber 6. Further, the result of lower oxygen was determined by analyzing each scaffolds' percent growth, percent viability, and gene expression. The results showed lower growth percentages and viability in downstream scaffolds. However, the use of hydrogel scaffolds greatly affected the growth and viability due to inconsistent contraction of the hydrogels. However, the general decrease in growth and viability confirmed a drop in oxygen saturation. A modified spheroid mathematical model was applied to estimate the volume of anoxic core regions in each scaffold. The model indicated larger anoxic core regions and a smaller depth to reach this anoxic core regions in downstream scaffolds. Although not a perfect match for the geometry of the collagen hydrogels, the model accounts for the oxygen concentration drop within hydrogel scaffolds. Lastly, the gene expression of crucial target genes for hypoxia regulation and disease progression and aggressiveness was analyzed using QRT-PCR. The results showed an increase in HIF-1α and downstream target genes in both chamber 1 and chamber 6. However, HIF-2α was downregulated in chamber 1 and chamber 2. The expression of these target genes confirms sub-saturation of oxygen in the downstream chambers. However, the increase in both chambers suggest potential cell signaling to chambers via the bulk media and metabolic adaptation of EMT6 cancer cells in sub-saturation oxygen levels.

In the future, this model could be modified to estimate the percent cell viability and growth on a per day basis to give a closer look at the viability, oxygen consumption, and growth of the scaffolds. This would more closely mimic the real time culture. The daily glucose consumption could be monitored from the media to provide additional insight into the metabolic activity. Additionally, histology and hypoxia staining should be conducted to verify the spheroid estimation model. Real time monitoring of the oxygen levels within the hydrogels at different depths can be monitored using microelectrodes could also be used for verification of oxygen levels [156]. To further ensure the model's accuracy, the PLLA mesh hydrogel holding scaffold should be modified to resemble a sphere, along with hydrogels being initially formed in the shape of a sphere. These adaptations will help the data better fit the geometry of the model for greater accuracy of estimations. Investigating different cell seeding values will help optimize the growth conditions that most closely represents a solid tumor without exceeding the upper limits of viable cell growth in the flow-perfusion bioreactor scaffold. The diffusion and release of cell signaling molecules, such as cytokines and cancer exosomes should be investigated and quantified. This will provide insight into potential genetic adaptations related to cancer cell stressed signaling. Lastly, this modified bioreactor should be seeded with MSCs to evaluate the effects of sub-saturation oxygen within a flow-perfusion bioreactor system.

2.6 References

[1] "Global cancer burden growing, amidst mounting need for services." Accessed: Mar. 14, 2025. [Online]. Available: https://www.who.int/news/item/01-02-2024-global-cancer-burden-growing--amidst-mounting-need-for-services

[2] "Cancer statistics, 2024 - Siegel - 2024 - CA: A Cancer Journal for Clinicians - Wiley Online Library." Accessed: Mar. 14, 2025. [Online]. Available: https://acsjournals.onlinelibrary.wiley.com/doi/10.3322/caac.21820

[3] "Insights on Cancer: Rates, Costs, and Strategies," NIHCM. Accessed: Mar. 27, 2025. [Online]. Available: https://nihcm.org/publications/insights-on-cancer-rates-costs-and-strategies?token=J9au_tHwvSj_cc3Nn9JrpuHQ96wJr6Bd

[4] F. Kreier, "Cancer will cost the world $25 trillion over next 30 years," *Nature*, Mar. 2023, doi: 10.1038/d41586-023-00634-9.

[5] A. B. Mariotto, L. Enewold, J. Zhao, C. A. Zeruto, and K. R. Yabroff, "Medical Care Costs Associated with Cancer Survivorship in the United States," *Cancer Epidemiol Biomarkers Prev*, vol. 29, no. 7, pp. 1304–1312, Jul. 2020, doi: 10.1158/1055-9965.EPI-19-1534.

[6] N. Iragorri, C. de Oliveira, N. Fitzgerald, and B. Essue, "The Out-of-Pocket Cost Burden of Cancer Care—A Systematic Literature Review," *Curr Oncol*, vol. 28, no. 2, pp. 1216–1248, Mar. 2021, doi: 10.3390/curroncol28020117.

[7] L. Collado and I. Brownell, "The crippling financial toxicity of cancer in the United States," *Cancer Biol Ther*, vol. 20, no. 10, pp. 1301–1303, Jul. 2019, doi: 10.1080/15384047.2019.1632132.

[8] J. S. de Moor, C. P. Williams, and V. S. Blinder, "Cancer-Related Care Costs and Employment Disruption: Recommendations to Reduce Patient Economic Burden as Part of Cancer Care Delivery," *JNCI Monographs*, vol. 2022, no. 59, pp. 79–84, Jul. 2022, doi: 10.1093/jncimonographs/lgac006.

[9] A. E. Yuzhalin, "Redefining cancer research for therapeutic breakthroughs," *Br J Cancer*, vol. 130, no. 7, pp. 1078–1082, Apr. 2024, doi: 10.1038/s41416-024-02634-6.

[10] M. Siddiqui and S. V. Rajkumar, "The High Cost of Cancer Drugs and What We Can Do About It," *Mayo Clin Proc*, vol. 87, no. 10, pp. 935–943, Oct. 2012, doi: 10.1016/j.mayocp.2012.07.007.

[11] S. Galarza, H. Kim, N. Atay, S. R. Peyton, and J. M. Munson, "2D or 3D? How cell motility measurements are conserved across dimensions in vitro and translate in vivo," *Bioeng Transl Med*, vol. 5, no. 1, p. e10148, Dec. 2019, doi: 10.1002/btm2.10148.

[12] F. Pampaloni, E. G. Reynaud, and E. H. K. Stelzer, "The third dimension bridges the gap between cell culture and live tissue," *Nat Rev Mol Cell Biol*, vol. 8, no. 10, pp. 839–845, Oct. 2007, doi: 10.1038/nrm2236.

[13] F. Berthiaume, P. V. Moghe, M. Toner, and M. L. Yarmush, "Effect of extracellular matrix topology on cell structure, function, and physiological responsiveness: hepatocytes cultured in a sandwich configuration," *FASEB J*, vol. 10, no. 13, pp. 1471–1484, Nov. 1996, doi: 10.1096/fasebj.10.13.8940293.

[14] A. Birgersdotter, R. Sandberg, and I. Ernberg, "Gene expression perturbation in vitro—A growing case for three-dimensional (3D) culture systems," *Seminars in Cancer Biology*, vol. 15, no. 5, pp. 405–412, Oct. 2005, doi: 10.1016/j.semcancer.2005.06.009.

[15] K. Duval *et al.*, "Modeling Physiological Events in 2D vs. 3D Cell Culture," *Physiology (Bethesda)*, vol. 32, no. 4, pp. 266–277, Jul. 2017, doi: 10.1152/physiol.00036.2016.

[16] M. Kapałczyńska *et al.*, "2D and 3D cell cultures – a comparison of different types of cancer cell cultures," *Arch Med Sci*, vol. 14, no. 4, pp. 910–919, Jun. 2018, doi: 10.5114/aoms.2016.63743.

[17] E. Knight and S. Przyborski, "Advances in 3D cell culture technologies enabling tissue-like structures to be created in vitro," *Journal of Anatomy*, vol. 227, no. 6, pp. 746–756, 2015, doi: 10.1111/joa.12257.

[18] T. S. Biju, V. V. Priya, and A. P. Francis, “Role of three-dimensional cell culture in therapeutics and diagnostics: an updated review,” *Drug Deliv. and Transl. Res.*, vol. 13, no. 9, pp. 2239–2253, Sep. 2023, doi: 10.1007/s13346-023-01327-6.
[19] A. van Rijt, E. Stefanek, and K. Valente, “Preclinical Testing Techniques: Paving the Way for New Oncology Screening Approaches,” *Cancers (Basel)*, vol. 15, no. 18, p. 4466, Sep. 2023, doi: 10.3390/cancers15184466.
[20] V. Foglizzo, E. Cocco, and S. Marchiò, “Advanced Cellular Models for Preclinical Drug Testing: From 2D Cultures to Organ-on-a-Chip Technology,” *Cancers (Basel)*, vol. 14, no. 15, p. 3692, Jul. 2022, doi: 10.3390/cancers14153692.
[21] R. Shyam, R. Singh, M. Bajpai, A. Palaniappan, and R. Parthasarathi, “Evolution of toxicity testing platforms from 2D to advanced 3D bioprinting for safety assessment of drugs,” *Bioprinting*, vol. 43, p. e00363, Nov. 2024, doi: 10.1016/j.bprint.2024.e00363.
[22] S. Martinez-Pacheco and L. O’Driscoll, “Pre-Clinical In Vitro Models Used in Cancer Research: Results of a Worldwide Survey,” *Cancers (Basel)*, vol. 13, no. 23, p. 6033, Nov. 2021, doi: 10.3390/cancers13236033.
[23] L. Belfiore *et al.*, “Generation and analysis of 3D cell culture models for drug discovery,” *European Journal of Pharmaceutical Sciences*, vol. 163, p. 105876, Aug. 2021, doi: 10.1016/j.ejps.2021.105876.
[24] R. D. Abbott and D. L. Kaplan, “Strategies for improving the physiological relevance of human engineered tissues,” *Trends Biotechnol*, vol. 33, no. 7, pp. 401–407, Jul. 2015, doi: 10.1016/j.tibtech.2015.04.003.
[25] C. Frantz, K. M. Stewart, and V. M. Weaver, “The extracellular matrix at a glance,” *J Cell Sci*, vol. 123, no. 24, pp. 4195–4200, Dec. 2010, doi: 10.1242/jcs.023820.
[26] R. Edmondson, J. J. Broglie, A. F. Adcock, and L. Yang, “Three-Dimensional Cell Culture Systems and Their Applications in Drug Discovery and Cell-Based Biosensors,” *Assay Drug Dev Technol*, vol. 12, no. 4, pp. 207–218, May 2014, doi: 10.1089/adt.2014.573.
[27] T. Michel *et al.*, “Mathematical modeling of the proliferation gradient in multicellular tumor spheroids,” *Journal of Theoretical Biology*, vol. 458, pp. 133–147, Dec. 2018, doi: 10.1016/j.jtbi.2018.08.031.
[28] “Metabolic Reprogramming and the Recovery of Physiological Functionality in 3D Cultures in Micro-Bioreactors.” Accessed: May 06, 2025. [Online]. Available: https://www.mdpi.com/2306-5354/5/1/22
[29] S. Mohan and R. Huneke, “The Role of IACUCs in Responsible Animal Research,” *ILAR J*, vol. 60, no. 1, pp. 43–49, Nov. 2019, doi: 10.1093/ilar/ilz016.
[30] F. E. Sharkey and J. Fogh, “Considerations in the use of nude mice for cancer research,” *Cancer Metastasis Rev*, vol. 3, no. 4, pp. 341–360, 1984, doi: 10.1007/BF00051459.
[31] L. R. Kelland, “Of mice and men: values and liabilities of the athymic nude mouse model in anticancer drug development,” *Eur J Cancer*, vol. 40, no. 6, pp. 827–836, Apr. 2004, doi: 10.1016/j.ejca.2003.11.028.
[32] H. Wang *et al.*, “3D cell culture models: Drug pharmacokinetics, safety assessment, and regulatory consideration,” *Clinical and Translational Science*, vol. 14, no. 5, pp. 1659–1680, 2021, doi: 10.1111/cts.13066.
[33] M. Peroglio, D. Gaspar, D. I. Zeugolis, and M. Alini, “Relevance of bioreactors and whole tissue cultures for the translation of new therapies to humans,” *Journal of Orthopaedic Research*, vol. 36, no. 1, pp. 10–21, 2018, doi: 10.1002/jor.23655.

[34] D. Antoni, H. Burckel, E. Josset, and G. Noel, “Three-Dimensional Cell Culture: A Breakthrough in Vivo,” *International Journal of Molecular Sciences*, vol. 16, no. 3, Art. no. 3, Mar. 2015, doi: 10.3390/ijms16035517.

[35] M. A. G. Barbosa, C. P. R. Xavier, R. F. Pereira, V. Petrikaitė, and M. H. Vasconcelos, “3D Cell Culture Models as Recapitulators of the Tumor Microenvironment for the Screening of Anti-Cancer Drugs,” *Cancers (Basel)*, vol. 14, no. 1, p. 190, Dec. 2021, doi: 10.3390/cancers14010190.

[36] B. Xue, J. Schüler, C. M. Harrod, K. Lashuk, Z. Bomya, and K. C. Hribar, “A Novel Hydrogel-Based 3D In Vitro Tumor Panel of 30 PDX Models Incorporates Tumor, Stromal and Immune Cell Compartments of the TME for the Screening of Oncology and Immuno-Therapies,” *Cells*, vol. 12, no. 8, p. 1145, Apr. 2023, doi: 10.3390/cells12081145.

[37] Z. N. Abbas, A. Z. Al-Saffar, S. M. Jasim, and G. M. Sulaiman, “Comparative analysis between 2D and 3D colorectal cancer culture models for insights into cellular morphological and transcriptomic variations,” *Sci Rep*, vol. 13, no. 1, p. 18380, Oct. 2023, doi: 10.1038/s41598-023-45144-w.

[38] Y. Fang and R. M. Eglen, “Three-Dimensional Cell Cultures in Drug Discovery and Development,” *SLAS Discov*, vol. 22, no. 5, pp. 456–472, Jun. 2017, doi: 10.1177/1087057117696795.

[39] F. J. O’Brien, “Biomaterials & scaffolds for tissue engineering,” *Materials Today*, vol. 14, no. 3, pp. 88–95, Mar. 2011, doi: 10.1016/S1369-7021(11)70058-X.

[40] A. J. Janvier, E. Canty-Laird, and J. R. Henstock, “A universal multi-platform 3D printed bioreactor chamber for tendon tissue engineering,” *J Tissue Eng*, vol. 11, p. 2041731420942462, Jan. 2020, doi: 10.1177/2041731420942462.

[41] C. Williams and T. M. Wick, “Perfusion Bioreactor for Small Diameter Tissue-Engineered Arteries,” *Tissue Engineering*, vol. 10, no. 5–6, pp. 930–941, May 2004, doi: 10.1089/1076327041348536.

[42] N. M. Anderson and M. C. Simon, “Tumor Microenvironment,” *Curr Biol*, vol. 30, no. 16, pp. R921–R925, Aug. 2020, doi: 10.1016/j.cub.2020.06.081.

[43] L.-B. Weiswald, D. Bellet, and V. Dangles-Marie, “Spherical Cancer Models in Tumor Biology,” *Neoplasia*, vol. 17, no. 1, pp. 1–15, Jan. 2015, doi: 10.1016/j.neo.2014.12.004.

[44] W. H. Abuwatfa, W. G. Pitt, and G. A. Husseini, “Scaffold-based 3D cell culture models in cancer research,” *Journal of Biomedical Science*, vol. 31, no. 1, p. 7, Jan. 2024, doi: 10.1186/s12929-024-00994-y.

[45] A. Bhattacharya *et al.*, “Exploring the interaction between extracellular matrix components in a 3D organoid disease model to replicate the pathophysiology of breast cancer,” *Journal of Experimental & Clinical Cancer Research*, vol. 42, no. 1, p. 343, Dec. 2023, doi: 10.1186/s13046-023-02926-4.

[46] S. M. Somers and W. L. Grayson, “Protocol for the Use of a Novel Bioreactor System for Hydrated Mechanical Testing, Strained Sterile Culture, and Force of Contraction Measurement of Tissue Engineered Muscle Constructs,” *Front. Cell Dev. Biol.*, vol. 9, Apr. 2021, doi: 10.3389/fcell.2021.661036.

[47] C. Jubelin *et al.*, “Three-dimensional in vitro culture models in oncology research,” *Cell & Bioscience*, vol. 12, no. 1, p. 155, Sep. 2022, doi: 10.1186/s13578-022-00887-3.

[48] “3D In Vitro Models for Investigating the Role of Stiffness in Cancer Invasion | ACS Biomaterials Science & Engineering.” Accessed: May 07, 2025. [Online]. Available: https://pubs.acs.org/doi/10.1021/acsbiomaterials.0c01530

[49] X. Morales, I. Cortés-Domínguez, and C. Ortiz-de-Solorzano, “Modeling the Mechanobiology of Cancer Cell Migration Using 3D Biomimetic Hydrogels,” *Gels*, vol. 7, no. 1, p. 17, Feb. 2021, doi: 10.3390/gels7010017.
[50] S. J. Bidarra, P. Oliveira, S. Rocha, D. P. Saraiva, C. Oliveira, and C. C. Barrias, “A 3D in vitro model to explore the inter-conversion between epithelial and mesenchymal states during EMT and its reversion,” *Sci Rep*, vol. 6, no. 1, p. 27072, Jun. 2016, doi: 10.1038/srep27072.
[51] M. Pal *et al.*, “Epithelial-mesenchymal transition of cancer cells using bioengineered hybrid scaffold composed of hydrogel/3D-fibrous framework,” *Sci Rep*, vol. 9, p. 8997, Jun. 2019, doi: 10.1038/s41598-019-45384-9.
[52] M. Majety, L. P. Pradel, M. Gies, and C. H. Ries, “Fibroblasts Influence Survival and Therapeutic Response in a 3D Co-Culture Model,” *PLOS ONE*, vol. 10, no. 6, p. e0127948, Jun. 2015, doi: 10.1371/journal.pone.0127948.
[53] M. R. Pandkar, S. G. Dhamdhere, and S. Shukla, “Oxygen gradient and tumor heterogeneity: The chronicle of a toxic relationship,” *Biochimica et Biophysica Acta (BBA) - Reviews on Cancer*, vol. 1876, no. 1, p. 188553, Aug. 2021, doi: 10.1016/j.bbcan.2021.188553.
[54] C. Liverani *et al.*, “A biomimetic 3D model of hypoxia-driven cancer progression,” *Sci Rep*, vol. 9, no. 1, p. 12263, Aug. 2019, doi: 10.1038/s41598-019-48701-4.
[55] J. Song, A. Miermont, C. T. Lim, and R. D. Kamm, “A 3D microvascular network model to study the impact of hypoxia on the extravasation potential of breast cell lines,” *Sci Rep*, vol. 8, no. 1, p. 17949, Dec. 2018, doi: 10.1038/s41598-018-36381-5.
[56] Y. Liu, Z. Mohri, W. Alsheikh, and U. Cheema, “The Role of Biomimetic Hypoxia on Cancer Cell Behaviour in 3D Models: A Systematic Review,” *Cancers*, vol. 13, no. 6, Art. no. 6, Jan. 2021, doi: 10.3390/cancers13061334.
[57] X. Jing *et al.*, “Role of hypoxia in cancer therapy by regulating the tumor microenvironment,” *Molecular Cancer*, vol. 18, no. 1, p. 157, Nov. 2019, doi: 10.1186/s12943-019-1089-9.
[58] A. Martinez *et al.*, “Utilization of a 3-D tissue engineered model to investigate the effects of perfusion on gynecologic cancer biology,” *J Tissue Eng*, vol. 12, p. 20417314211055015, Jan. 2021, doi: 10.1177/20417314211055015.
[59] C. Hirt *et al.*, “Bioreactor-engineered cancer tissue-like structures mimic phenotypes, gene expression profiles and drug resistance patterns observed ‘in vivo,’” *Biomaterials*, vol. 62, pp. 138–146, Sep. 2015, doi: 10.1016/j.biomaterials.2015.05.037.
[60] Z. Peng, X. Lv, H. Sun, L. Zhao, and S. Huang, “3D tumor cultures for drug resistance and screening development in clinical applications,” *Molecular Cancer*, vol. 24, no. 1, p. 93, Mar. 2025, doi: 10.1186/s12943-025-02281-2.
[61] C. Sordo-Bahamonde *et al.*, “Chemo-Immunotherapy: A New Trend in Cancer Treatment,” *Cancers (Basel)*, vol. 15, no. 11, p. 2912, May 2023, doi: 10.3390/cancers15112912.
[62] K. Balážová, H. Clevers, and A. F. Dost, “The role of macrophages in non-small cell lung cancer and advancements in 3D co-cultures,” *eLife*, vol. 12, p. e82998, Feb. 2023, doi: 10.7554/eLife.82998.
[63] S.-R. Jeong and M. Kang, “Exploring Tumor–Immune Interactions in Co-Culture Models of T Cells and Tumor Organoids Derived from Patients,” *International Journal of Molecular Sciences*, vol. 24, no. 19, Art. no. 19, Jan. 2023, doi: 10.3390/ijms241914609.

[64] D. P. Saraiva, A. T. Matias, S. Braga, A. Jacinto, and M. G. Cabral, "Establishment of a 3D Co-culture With MDA-MB-231 Breast Cancer Cell Line and Patient-Derived Immune Cells for Application in the Development of Immunotherapies," *Front. Oncol.*, vol. 10, Aug. 2020, doi: 10.3389/fonc.2020.01543.
[65] O. Candini *et al.*, "A Novel 3D In Vitro Platform for Pre-Clinical Investigations in Drug Testing, Gene Therapy, and Immuno-oncology," *Sci Rep*, vol. 9, no. 1, p. 7154, May 2019, doi: 10.1038/s41598-019-43613-9.
[66] C. Selden and B. Fuller, "Role of Bioreactor Technology in Tissue Engineering for Clinical Use and Therapeutic Target Design," *Bioengineering (Basel)*, vol. 5, no. 2, p. 32, Apr. 2018, doi: 10.3390/bioengineering5020032.
[67] M. C. McCorry *et al.*, "Sensor technologies for quality control in engineered tissue manufacturing," *Biofabrication*, vol. 15, no. 1, p. 10.1088/1758-5090/ac94a1, Oct. 2022, doi: 10.1088/1758-5090/ac94a1.
[68] N. Plunkett and F. O'Brien, "IV.3. Bioreactors in tissue engineering," *Technology and health care : official journal of the European Society for Engineering and Medicine*, vol. 19, pp. 55–69, Jan. 2011, doi: 10.3233/THC-2011-0605.
[69] F. Palladino *et al.*, "Bioreactors: Applications and Innovations for a Sustainable and Healthy Future—A Critical Review," *Applied Sciences*, vol. 14, no. 20, Art. no. 20, Jan. 2024, doi: 10.3390/app14209346.
[70] E. T. Duman, A. Kose, Y. Celik, and S. S. Oncel, "Design of a horizontal-dual bladed bioreactor for low shear stress to improve hydrodynamic responses in cell cultures: A pilot study in *Chlamydomonas reinhardtii*," *Biochemical Engineering Journal*, vol. 169, p. 107970, May 2021, doi: 10.1016/j.bej.2021.107970.
[71] E. Costariol *et al.*, "Demonstrating the Manufacture of Human CAR-T Cells in an Automated Stirred-Tank Bioreactor," *Biotechnology Journal*, vol. 15, no. 9, p. 2000177, 2020, doi: 10.1002/biot.202000177.
[72] M. Guo, Z. Yin, F. Chen, and P. Lei, "Mesenchymal stem cell-derived exosome: A promising alternative in the therapy of Alzheimer's disease," *Alzheimer's research & therapy*, vol. 12, p. 109, Dec. 2020, doi: 10.1186/s13195-020-00670-x.
[73] S. Talukdar and S. C. Kundu, "18 - Silk scaffolds for three-dimensional (3D) tumor modeling," in *Silk Biomaterials for Tissue Engineering and Regenerative Medicine*, S. C. Kundu, Ed., Woodhead Publishing, 2014, pp. 472–502. doi: 10.1533/9780857097064.3.472.
[74] M. Campbell, L. Surija, K. Peceros, P. Sharma, G. Figtree, and C. Gentile, "Stem Cell Spheroids," in *Encyclopedia of Tissue Engineering and Regenerative Medicine*, R. L. Reis, Ed., Oxford: Academic Press, 2019, pp. 387–393. doi: 10.1016/B978-0-12-801238-3.65536-8.
[75] P. Sucosky, D. F. Osorio, J. B. Brown, and G. P. Neitzel, "Fluid mechanics of a spinner-flask bioreactor," *Biotechnol Bioeng*, vol. 85, no. 1, pp. 34–46, Jan. 2004, doi: 10.1002/bit.10788.
[76] J. K. Gardner and M. M. Herbst-Kralovetz, "Three-Dimensional Rotating Wall Vessel-Derived Cell Culture Models for Studying Virus-Host Interactions," *Viruses*, vol. 8, no. 11, p. 304, Nov. 2016, doi: 10.3390/v8110304.
[77] A. L. Radtke and M. M. Herbst-Kralovetz, "Culturing and Applications of Rotating Wall Vessel Bioreactor Derived 3D Epithelial Cell Models," *J Vis Exp*, no. 62, p. 3868, Apr. 2012, doi: 10.3791/3868.

[78] J. Barrila *et al.*, “Organotypic 3D cell culture models: using the rotating wall vessel to study host–pathogen interactions,” *Nat Rev Microbiol*, vol. 8, no. 11, pp. 791–801, Nov. 2010, doi: 10.1038/nrmicro2423.
[79] A. Graham *et al.*, “Design and construction of a low-cost compressive loading and perfusion flow bioreactor,” *HardwareX*, vol. 19, p. e00565, Sep. 2024, doi: 10.1016/j.ohx.2024.e00565.
[80] T. Wang *et al.*, “Bioreactor Design for Tendon/Ligament Engineering,” *Tissue engineering. Part B, Reviews*, vol. 19, Oct. 2012, doi: 10.1089/ten.TEB.2012.0295.
[81] B. Rath, J. Nam, T. J. Knobloch, J. J. Lannutti, and S. Agarwal, “Compressive forces induce osteogenic gene expression in calvarial osteoblasts,” *J Biomech*, vol. 41, no. 5, pp. 1095–1103, 2008, doi: 10.1016/j.jbiomech.2007.11.024.
[82] D. L. Butler *et al.*, “Using Functional Tissue Engineering and Bioreactors to Mechanically Stimulate Tissue-Engineered Constructs,” *Tissue Eng Part A*, vol. 15, no. 4, pp. 741–749, Apr. 2009, doi: 10.1089/ten.tea.2008.0292.
[83] S. J. Reyes, Y. Durocher, P. L. Pham, and O. Henry, “Modern Sensor Tools and Techniques for Monitoring, Controlling, and Improving Cell Culture Processes,” *Processes*, vol. 10, no. 2, Art. no. 2, Feb. 2022, doi: 10.3390/pr10020189.
[84] C. Busse, P. Biechele, I. de Vries, K. F. Reardon, D. Solle, and T. Scheper, “Sensors for disposable bioreactors,” *Eng Life Sci*, vol. 17, no. 8, pp. 940–952, Aug. 2017, doi: 10.1002/elsc.201700049.
[85] M. Hoenicka, L. Wiedemann, T. Puehler, S. Hirt, D. E. Birnbaum, and C. Schmid, “Effects of Shear Forces and Pressure on Blood Vessel Function and Metabolism in a Perfusion Bioreactor,” *Ann Biomed Eng*, vol. 38, no. 12, pp. 3706–3723, Dec. 2010, doi: 10.1007/s10439-010-0116-1.
[86] E. Pishavar *et al.*, “Advanced Hydrogels as Exosome Delivery Systems for Osteogenic Differentiation of MSCs: Application in Bone Regeneration,” *Int J Mol Sci*, vol. 22, no. 12, p. 6203, Jun. 2021, doi: 10.3390/ijms22126203.
[87] J. N. Harvestine *et al.*, “Osteogenic preconditioning in perfusion bioreactors improves vascularization and bone formation by human bone marrow aspirates,” *Sci Adv*, vol. 6, no. 7, p. eaay2387, Feb. 2020, doi: 10.1126/sciadv.aay2387.
[88] D. A. Gaspar, V. Gomide, and F. J. Monteiro, “The role of perfusion bioreactors in bone tissue engineering,” *Biomatter*, vol. 2, no. 4, pp. 167–175, Oct. 2012, doi: 10.4161/biom.22170.
[89] N. Salehi-Nik *et al.*, “Engineering Parameters in Bioreactor’s Design: A Critical Aspect in Tissue Engineering,” *Biomed Res Int*, vol. 2013, p. 762132, 2013, doi: 10.1155/2013/762132.
[90] J. Meneses, S. R. Fernandes, J. C. Silva, F. C. Ferreira, N. Alves, and P. Pascoal-Faria, “JANUS: an open-source 3D printable perfusion bioreactor and numerical model-based design strategy for tissue engineering,” *Front. Bioeng. Biotechnol.*, vol. 11, Dec. 2023, doi: 10.3389/fbioe.2023.1308096.
[91] V. Foglizzo, E. Cocco, and S. Marchiò, “Advanced Cellular Models for Preclinical Drug Testing: From 2D Cultures to Organ-on-a-Chip Technology,” *Cancers (Basel)*, vol. 14, no. 15, p. 3692, Jul. 2022, doi: 10.3390/cancers14153692.
[92] S. Halldorsson, E. Lucumi, R. Gómez-Sjöberg, and R. M. T. Fleming, “Advantages and challenges of microfluidic cell culture in polydimethylsiloxane devices,” *Biosensors and Bioelectronics*, vol. 63, pp. 218–231, Jan. 2015, doi: 10.1016/j.bios.2014.07.029.

[93] C. Lucas, M. Blackman, A. Rayat, D. Mainwaring, and M. Micheletti, “Two scale-down tools for the optimization of perfusion bioreactors for the manufacture of biopharmaceuticals,” *Journal of Advanced Manufacturing and Processing*, vol. 6, no. 3, p. e10180, 2024, doi: 10.1002/amp2.10180.
[94] Z. Fang *et al.*, “Application of bioreactor technology for cell culture-based viral vaccine production: Present status and future prospects,” *Front Bioeng Biotechnol*, vol. 10, p. 921755, Aug. 2022, doi: 10.3389/fbioe.2022.921755.
[95] A. L. Zydney, “Perspectives on integrated continuous bioprocessing — opportunities and challenges,” *Current Opinion in Chemical Engineering*, vol. 10, pp. 8–13, Nov. 2015, doi: 10.1016/j.coche.2015.07.005.
[96] N. H. Bishopric *et al.*, “Hypoxia-activated apoptosis of cardiac myocytes requires reoxygenation or a pH shift and is independent of p53,” *J Clin Invest*, vol. 104, no. 3, pp. 239–252, Aug. 1999, doi: 10.1172/JCI5871.
[97] Y. Chen, E. McMillan-Ward, J. Kong, S. J. Israels, and S. B. Gibson, “Oxidative stress induces autophagic cell death independent of apoptosis in transformed and cancer cells,” *Cell Death Differ*, vol. 15, no. 1, pp. 171–182, Jan. 2008, doi: 10.1038/sj.cdd.4402233.
[98] Y. Guo, J. Tan, Y. Miao, Z. Sun, and Q. Zhang, “Effects of Microvesicles on Cell Apoptosis under Hypoxia,” *Oxid Med Cell Longev*, vol. 2019, p. 5972152, Apr. 2019, doi: 10.1155/2019/5972152.
[99] F. Hakim *et al.*, “High Oxygen Condition Facilitates the Differentiation of Mouse and Human Pluripotent Stem Cells into Pancreatic Progenitors and Insulin-producing Cells,” *J Biol Chem*, vol. 289, no. 14, pp. 9623–9638, Apr. 2014, doi: 10.1074/jbc.M113.524363.
[100] H. Abdollahi, L. J. Harris, P. Zhang, S. McIlhenny, T. Tulenko, and P. J. DiMuzio, “The Role of Hypoxia in Stem Cell Differentiation and Therapeutics,” *J Surg Res*, vol. 165, no. 1, pp. 112–117, Jan. 2011, doi: 10.1016/j.jss.2009.09.057.
[101] K. Nit, M. Tyszka-Czochara, and S. Bobis-Wozowicz, “Oxygen as a Master Regulator of Human Pluripotent Stem Cell Function and Metabolism,” *J Pers Med*, vol. 11, no. 9, p. 905, Sep. 2021, doi: 10.3390/jpm11090905.
[102] T. Rademakers, J. M. Horvath, C. A. van Blitterswijk, and V. L. S. LaPointe, “Oxygen and nutrient delivery in tissue engineering: Approaches to graft vascularization,” *J Tissue Eng Regen Med*, vol. 13, no. 10, pp. 1815–1829, Oct. 2019, doi: 10.1002/term.2932.
[103] J. J. Kim, L. Hou, and N. F. Huang, “Vascularization of Three-Dimensional Engineered Tissues for Regenerative Medicine Applications,” *Acta Biomater*, vol. 41, pp. 17–26, Sep. 2016, doi: 10.1016/j.actbio.2016.06.001.
[104] S. Suvarnapathaki, X. Wu, D. Lantigua, M. A. Nguyen, and G. Camci-Unal, “Breathing life into engineered tissues using oxygen-releasing biomaterials,” *NPG Asia Mater*, vol. 11, no. 1, pp. 1–18, Nov. 2019, doi: 10.1038/s41427-019-0166-2.
[105] Z. Zhu *et al.*, “Microfluidic strategies for engineering oxygen-releasing biomaterials,” *Acta Biomaterialia*, vol. 179, pp. 61–82, Apr. 2024, doi: 10.1016/j.actbio.2024.03.032.
[106] D. W. Siemann, “The Unique Characteristics of Tumor Vasculature and Preclinical Evidence for its Selective Disruption by Tumor-Vascular Disrupting Agents,” *Cancer Treat Rev*, vol. 37, no. 1, pp. 63–74, Feb. 2011, doi: 10.1016/j.ctrv.2010.05.001.
[107] N. S. Awad, N. M. Salkho, W. H. Abuwatfa, V. Paul, N. M. AlSawaftah, and G. A. Husseini, “Tumor vasculature vs tumor cell targeting: Understanding the latest trends in using functional nanoparticles for cancer treatment,” *OpenNano*, vol. 11, p. 100136, May 2023, doi: 10.1016/j.onano.2023.100136.

[108] S. Ferretti, P. R. Allegrini, M. M. Becquet, and P. M. McSheehy, “Tumor Interstitial Fluid Pressure as an Early-Response Marker for Anticancer Therapeutics,” *Neoplasia*, vol. 11, no. 9, pp. 874–881, Sep. 2009, doi: 10.1593/neo.09554.
[109] M. Milosevic *et al.*, “Interstitial Fluid Pressure Predicts Survival in Patients with Cervix Cancer Independent of Clinical Prognostic Factors and Tumor Oxygen Measurements1,” *Cancer Research*, vol. 61, no. 17, pp. 6400–6405, Sep. 2001.
[110] S. K. Libutti, L. Tamarkin, and N. Nilubol, “Targeting the invincible barrier for drug delivery in solid cancers: interstitial fluid pressure,” *Oncotarget*, vol. 9, no. 87, pp. 35723–35725, Nov. 2018, doi: 10.18632/oncotarget.26267.
[111] Q. Yang, N. Guo, Y. Zhou, J. Chen, Q. Wei, and M. Han, “The role of tumor-associated macrophages (TAMs) in tumor progression and relevant advance in targeted therapy,” *Acta Pharm Sin B*, vol. 10, no. 11, pp. 2156–2170, Nov. 2020, doi: 10.1016/j.apsb.2020.04.004.
[112] “Roles of macrophages in tumor development: a spatiotemporal perspective | Cellular & Molecular Immunology.” Accessed: Jun. 18, 2025. [Online]. Available: https://www.nature.com/articles/s41423-023-01061-6
[113] R. Huang, T. Kang, and S. Chen, “The role of tumor-associated macrophages in tumor immune evasion,” *J Cancer Res Clin Oncol*, vol. 150, no. 5, p. 238, 2024, doi: 10.1007/s00432-024-05777-4.
[114] A. Xia, Y. Zhang, J. Xu, T. Yin, and X.-J. Lu, “T Cell Dysfunction in Cancer Immunity and Immunotherapy,” *Front Immunol*, vol. 10, p. 1719, Jul. 2019, doi: 10.3389/fimmu.2019.01719.
[115] Y. Arima, S. Matsueda, and H. Saya, “Significance of Cancer-Associated Fibroblasts in the Interactions of Cancer Cells with the Tumor Microenvironment of Heterogeneous Tumor Tissue,” *Cancers (Basel)*, vol. 15, no. 9, p. 2536, Apr. 2023, doi: 10.3390/cancers15092536.
[116] B. Erdogan and D. J. Webb, “Cancer-associated fibroblasts modulate growth factor signaling and extracellular matrix remodeling to regulate tumor metastasis,” *Biochem Soc Trans*, vol. 45, no. 1, pp. 229–236, Feb. 2017, doi: 10.1042/BST20160387.
[117] S. Chen *et al.*, “Cancer-associated fibroblast-induced M2-polarized macrophages promote hepatocellular carcinoma progression via the plasminogen activator inhibitor-1 pathway,” *Int J Oncol*, vol. 59, no. 2, p. 59, Jul. 2021, doi: 10.3892/ijo.2021.5239.
[118] M. V. Liberti and J. W. Locasale, “The Warburg Effect: How Does it Benefit Cancer Cells?,” *Trends in Biochemical Sciences*, vol. 41, no. 3, pp. 211–218, Mar. 2016, doi: 10.1016/j.tibs.2015.12.001.
[119] M. Mathew, N. T. Nguyen, Y. D. Bhutia, S. Sivaprakasam, and V. Ganapathy, “Metabolic Signature of Warburg Effect in Cancer: An Effective and Obligatory Interplay between Nutrient Transporters and Catabolic/Anabolic Pathways to Promote Tumor Growth,” *Cancers*, vol. 16, no. 3, Art. no. 3, Jan. 2024, doi: 10.3390/cancers16030504.
[120] M. Jaworska *et al.*, “The Warburg effect: a score for many instruments in the concert of cancer and cancer niche cells,” *Pharmacol Rep*, vol. 75, no. 4, pp. 876–890, 2023, doi: 10.1007/s43440-023-00504-1.
[121] H. Kang, B. Kim, J. Park, H. Youn, and B. Youn, “The Warburg effect on radioresistance: Survival beyond growth,” *Biochimica et Biophysica Acta (BBA) - Reviews on Cancer*, vol. 1878, no. 6, p. 188988, Nov. 2023, doi: 10.1016/j.bbcan.2023.188988.

[122] P. Vaupel, H. Schmidberger, and A. Mayer, “The Warburg effect: essential part of metabolic reprogramming and central contributor to cancer progression,” *Int J Radiat Biol*, vol. 95, no. 7, pp. 912–919, Jul. 2019, doi: 10.1080/09553002.2019.1589653.
[123] “Cancer metabolism and the Warburg effect: the role of HIF-1 and PI3K | Molecular Biology Reports.” Accessed: Jun. 16, 2025. [Online]. Available: https://link.springer.com/article/10.1007/s11033-015-3858-x
[124] C. Zhang *et al.*, “Tumor-Associated Mutant p53 Drives the Warburg Effect,” *Nat Commun*, vol. 4, p. 2935, 2013, doi: 10.1038/ncomms3935.
[125] “Epithelial-mesenchymal Transition and Cancer Stem Cells: At the Crossroads of Differentiation and Dedifferentiation - Wang - 2019 - Developmental Dynamics - Wiley Online Library.” Accessed: Jun. 18, 2025. [Online]. Available: https://anatomypubs.onlinelibrary.wiley.com/doi/10.1002/dvdy.24678
[126] Y. Huang, W. Hong, and X. Wei, “The molecular mechanisms and therapeutic strategies of EMT in tumor progression and metastasis,” *Journal of Hematology & Oncology*, vol. 15, no. 1, p. 129, Sep. 2022, doi: 10.1186/s13045-022-01347-8.
[127] T. Liao and M. Yang, “Revisiting epithelial-mesenchymal transition in cancer metastasis: the connection between epithelial plasticity and stemness,” *Mol Oncol*, vol. 11, no. 7, pp. 792–804, Jul. 2017, doi: 10.1002/1878-0261.12096.
[128] Z. Chen, F. Han, Y. Du, H. Shi, and W. Zhou, “Hypoxic microenvironment in cancer: molecular mechanisms and therapeutic interventions,” *Sig Transduct Target Ther*, vol. 8, no. 1, pp. 1–23, Feb. 2023, doi: 10.1038/s41392-023-01332-8.
[129] A. Emami Nejad *et al.*, “The role of hypoxia in the tumor microenvironment and development of cancer stem cell: a novel approach to developing treatment,” *Cancer Cell International*, vol. 21, no. 1, p. 62, Jan. 2021, doi: 10.1186/s12935-020-01719-5.
[130] J. E. Ziello, I. S. Jovin, and Y. Huang, “Hypoxia-Inducible Factor (HIF)-1 Regulatory Pathway and its Potential for Therapeutic Intervention in Malignancy and Ischemia,” *Yale J Biol Med*, vol. 80, no. 2, pp. 51–60, Jun. 2007.
[131] A. Weidemann and R. S. Johnson, “Biology of HIF-1α,” *Cell Death Differ*, vol. 15, no. 4, pp. 621–627, Apr. 2008, doi: 10.1038/cdd.2008.12.
[132] J. C. Jun, A. Rathore, H. Younas, D. Gilkes, and V. Y. Polotsky, “Hypoxia-Inducible Factors and Cancer,” *Curr Sleep Med Rep*, vol. 3, no. 1, pp. 1–10, Mar. 2017, doi: 10.1007/s40675-017-0062-7.
[133] M. Jaśkiewicz *et al.*, “The transition from HIF-1 to HIF-2 during prolonged hypoxia results from reactivation of PHDs and HIF1A mRNA instability,” *Cellular & Molecular Biology Letters*, vol. 27, no. 1, p. 109, Dec. 2022, doi: 10.1186/s11658-022-00408-7.
[134] C. W. Song *et al.*, “Role of HIF-1α in the Responses of Tumors to Radiotherapy and Chemotherapy,” *Cancer Res Treat*, vol. 57, no. 1, pp. 1–10, Jan. 2025, doi: 10.4143/crt.2024.255.
[135] G. Multhoff and P. Vaupel, “Hypoxia Compromises Anti-Cancer Immune Responses,” in *Oxygen Transport to Tissue XLI*, P.-D. Ryu, J. C. LaManna, D. K. Harrison, and S.-S. Lee, Eds., Cham: Springer International Publishing, 2020, pp. 131–143. doi: 10.1007/978-3-030-34461-0_18.
[136] J. Liu, Y. Jiang, L. Chen, Z. Qian, and Y. Zhang, “Associations between HIFs and tumor immune checkpoints: mechanism and therapy,” *Discov Onc*, vol. 15, no. 1, p. 2, Jan. 2024, doi: 10.1007/s12672-023-00836-7.

[137] G. L. Semenza, “HIF-1: upstream and downstream of cancer metabolism,” *Current opinion in genetics & development*, vol. 20, no. 1, p. 51, Nov. 2009, doi: 10.1016/j.gde.2009.10.009.
[138] E. E. Wicks and G. L. Semenza, “Hypoxia-inducible factors: cancer progression and clinical translation,” *J Clin Invest*, vol. 132, no. 11, p. e159839, doi: 10.1172/JCI159839.
[139] V. Infantino, A. Santarsiero, P. Convertini, S. Todisco, and V. Iacobazzi, “Cancer Cell Metabolism in Hypoxia: Role of HIF-1 as Key Regulator and Therapeutic Target,” *International Journal of Molecular Sciences*, vol. 22, no. 11, p. 5703, May 2021, doi: 10.3390/ijms22115703.
[140] E. C. de Heer, M. Jalving, and A. L. Harris, “HIFs, angiogenesis, and metabolism: elusive enemies in breast cancer,” *J Clin Invest*, vol. 130, no. 10, pp. 5074–5087, doi: 10.1172/JCI137552.
[141] P. W. T. Lee, L. R. Koseki, T. Haitani, H. Harada, and M. Kobayashi, “Hypoxia-Inducible Factor-Dependent and Independent Mechanisms Underlying Chemoresistance of Hypoxic Cancer Cells,” *Cancers*, vol. 16, no. 9, p. 1729, Apr. 2024, doi: 10.3390/cancers16091729.
[142] N. Rohwer and T. Cramer, “Hypoxia-mediated drug resistance: Novel insights on the functional interaction of HIFs and cell death pathways,” *Drug Resistance Updates*, vol. 14, no. 3, pp. 191–201, Jun. 2011, doi: 10.1016/j.drup.2011.03.001.
[143] Y. Zhao, C. Xing, Y. Deng, C. Ye, and H. Peng, “HIF-1α signaling: Essential roles in tumorigenesis and implications in targeted therapies,” *Genes & Diseases*, vol. 11, no. 1, pp. 234–251, Jan. 2024, doi: 10.1016/j.gendis.2023.02.039.
[144] P. Bryant, “Utilizing Flow Perfusion Bioreactor Systems as Novel Platforms for Cancer Research,” Aug. 2023, Accessed: May 13, 2025. [Online]. Available: https://shareok.org/handle/11244/337951
[145] A. D. Simmons and V. I. Sikavitsas, “Monitoring Bone Tissue Engineered (BTE) Constructs Based on the Shifting Metabolism of Differentiating Stem Cells,” *Ann Biomed Eng*, vol. 46, no. 1, pp. 37–47, Jan. 2018, doi: 10.1007/s10439-017-1937-y.
[146] “(PDF) Compilation of Henry’s law constants (Version 4.0) for water as solvent.” Accessed: May 13, 2025. [Online]. Available: https://www.researchgate.net/publication/277346419_Compilation_of_Henry's_law_constants_Version_40_for_water_as_solvent
[147] M. L. Felder, A. D. Simmons, R. L. Shambaugh, and V. I. Sikavitsas, “Effects of Flow Rate on Mesenchymal Stem Cell Oxygen Consumption Rates in 3D Bone-Tissue-Engineered Constructs Cultured in Perfusion Bioreactor Systems,” *Fluids*, vol. 5, no. 1, Art. no. 1, Mar. 2020, doi: 10.3390/fluids5010030.
[148] D. R. Grimes, C. Kelly, K. Bloch, and M. Partridge, “A method for estimating the oxygen consumption rate in multicellular tumour spheroids,” *J R Soc Interface*, vol. 11, no. 92, p. 20131124, Mar. 2014, doi: 10.1098/rsif.2013.1124.
[149] A. Colom, R. Galgoczy, I. Almendros, A. Xaubet, R. Farré, and J. Alcaraz, “Oxygen diffusion and consumption in extracellular matrix gels: implications for designing three-dimensional cultures,” *J Biomed Mater Res A*, vol. 102, no. 8, pp. 2776–2784, Aug. 2014, doi: 10.1002/jbm.a.34946.
[150] D. Lam *et al.*, “Optimizing cell encapsulation condition in ECM-Collagen I hydrogels to support 3D neuronal cultures,” *Journal of Neuroscience Methods*, vol. 329, p. 108460, Jan. 2020, doi: 10.1016/j.jneumeth.2019.108460.

[151] “An overview of bio-actuation in collagen hydrogels: a mechanobiological phenomenon - PubMed.” Accessed: Jul. 03, 2025. [Online]. Available: https://pubmed.ncbi.nlm.nih.gov/34178172/
[152] F. P. Duda, A. C. Souza, and E. Fried, “Fluid flow and interface motion in gels: A finite-strain theory and its application to a channel flow problem,” *Journal of the Mechanics and Physics of Solids*, vol. 155, p. 104566, Oct. 2021, doi: 10.1016/j.jmps.2021.104566.
[153] C. Mehner, E. Miller, A. Nassar, W. R. Bamlet, E. S. Radisky, and D. C. Radisky, “Tumor cell expression of MMP3 as a prognostic factor for poor survival in pancreatic, pulmonary, and mammary carcinoma,” *Genes Cancer*, vol. 6, no. 11–12, pp. 480–489, Nov. 2015, doi: 10.18632/genesandcancer.90.
[154] C. J. Foley, C. Luo, K. O’Callaghan, P. W. Hinds, L. Covic, and A. Kuliopulos, “Matrix Metalloprotease-1a Promotes Tumorigenesis and Metastasis,” *J Biol Chem*, vol. 287, no. 29, pp. 24330–24338, Jul. 2012, doi: 10.1074/jbc.M112.356303.
[155] Y. Han, D. Liu, and L. Li, “PD-1/PD-L1 pathway: current researches in cancer,” *Am J Cancer Res*, vol. 10, no. 3, pp. 727–742, Mar. 2020.
[156] K. C. Murphy *et al.*, “Measurement of oxygen tension within mesenchymal stem cell spheroids,” *J. R. Soc. Interface.*, vol. 14, no. 127, p. 20160851, Feb. 2017, doi: 10.1098/rsif.2016.0851.